# Fabrication and Characterization of Superconducting Core Fibers with Fused Silica Cladding

Yongxuan Liang

Thesis submitted to the faculty of the Virginia Polytechnic Institute and State University in partial fulfillment of the requirements for the degree of

Master of Science

In

Materials Science and Engineering

Gary R. Pickrell, Chair

David E. Clark

Daniel S. Homa

January 29, 2014
Blacksburg, VA

Keywords: Fiber, Superconducting core, Melt-draw, Microstructure, Four-probe, Efficient cooling, Heat transfer

# Fabrication and Characterization of Superconducting Core Fibers with Fused Silica Cladding

Yongxuan Liang

ABSTRACT

Since the discovery of superconductivity, its fantastic properties have fascinated the scientific community. The discovery of high critical temperature ($T_c$) superconducting compositions further inspires the wide applications of superconductors with relatively inexpensive liquid nitrogen cooling. Recently, the integration of superconductivity and optical waveguides has put forward the potential for ultrasensitive, ultra-fast and ultralow noise light detectors. However, simple and cost effective superconductor designs and fabrication processes are still required to enable wide implementation. The objective of this research was to study the fabrication of the superconductor core fibers with a fused silica cladding via the melt-draw approach, as well as develop appropriate characterization techniques to describe the fibers produced. In addition, a further objective was to determine the cooling efficiency of ordered holes around a superconductor core and construction of a one dimensional (1-D) single-phase steady state model to predict the heat transfer during cryogenic liquid transfer inside glass tube. In this thesis, both Pb and YBCO superconductor core fibers with fused silica cladding have been demonstrated. The fibers were fabricated via the melt-draw technique and maintained overall diameters ranging from 200-900 μm and core diameters of 100-800 μm. Surface morphology, chemical composition, interface effect, and superconductivity were further investigated. Surface morphology analysis confirmed that the Pb and YBCO core fibers possessed good circularity and clean interfaces between the core and cladding. Both the Pb and YBCO cores were relatively dense after the melt-draw process. The melt-draw process avoided contamination during fabrication as indicated by the composition analysis. Limited PbO was examined on the Pb core surface but further action will be required to detect the source of oxygen. The YBCO core maintained a stoichiometric ratio comparable to the superconducting phase even after the melt forming process. The elemental mapping showed that limited cross-diffusion occurred between the Pb core and fused silica cladding. Conversely significantly more elemental cross interaction between the core and cladding was noted for the YBCO core fiber. Superconductivity of the Pb core was verified by a custom designed four-probe technique in liquid helium. The YBCO core was also confirmed to be superconductive after heat treatment with $O_2$ present. The feasibility of efficient cooling by the holey glass tubes was confirmed. A 1-D single-phase steady state model was constructed to evaluate the heat transfer mechanism. The experimental results are in reasonable agreement to the theoretical calculation.

# Acknowledgements

First and foremost I would like to thank my advisor and the committee chair, Dr. Gary Pickrell, a fantastic supervisor with sharp intellect, for providing me this precious opportunity. I learnt from him not only the critical thinking but also how to plan things wisely. Without his invaluable support and patient guidance, this thesis can't be completed such efficient.

I am also indebted to Dr. Daniel Homa. His hard working and persistence inspired me to solve all kinds of technical obstacles. He taught me to never look down on myself and always keep the faith in the pursuit of success. Every day working with him is a memorable experience.

I am also very grateful to Dr. David Clark for his precious time, valuable suggestions, insightful criticism and support.

I am also thankful to members in my research group fellows, Dr. Brian Scott, Dr. Gurbinder Kaur, Adam Floyd, Cary Hill, Taylor Blair, Yujie Cheng, Robert Mills. Thanks for their friendship and help.

I also would like to thank Dr. Jean Joseph Heremans and Yao Zhang from Department of Physics in Virginia Tech for their patience and invaluable assistance with our experimentation.

Also put my sincerely grateful to my parents and my wife Jingyi Yin for their continuous encouragement and lovable support.

## Table of contents

## List of Figures

## List of Tables

# 1 Introduction

## 1.1 Motivation and objective

Superconductive materials have recently undergone renewed interest because of their potential to significantly benefit society[1]. Significant effort has been directed on the fundamental understanding of the phenomena, as well the applied research in the power transmission and sensing applications[2, 3]. The discoveries of high critical temperature ($T_c$) superconducting compositions further inspired the wide applications of superconductors with the relatively inexpensive liquid nitrogen cooling. Recently, the integration of superconductivity and optical waveguides was proposed for ultrasensitive, ultra-fast and ultralow noise light detectors[4-6]. Unfortunately, the brittleness and fragility for some ceramic superconducting compositions inhibit their usability. Therefore, simple and cost effective superconductor designs and fabrication processes are required to enable wide implementation. The mature manufacturing of optical fibers can provide us a simple and cost effective way to realize this goal.

The objective of this study is to realize the fabrication of the superconductor core fibers with silica cladding via the melt-draw approach, as well as the appropriate characterization to describe the fiber prepared. Furthermore, efficient cooling with the ordered holes around the superconductor core was studied and a one dimensional (1-D) single-phase steady state model to predict the heat transfer during cryogenic liquid transfer inside the glass tube was developed.

## 1.2 Technical routes

In this research, we developed the experimental process to demonstrate the superconductor core fiber. A low temperature superconductor, Pb ($T_c$=7.2 K), and a high temperature superconductor, YBCO (1-2-3) ($T_c$=93 K), were used as the starting materials. Pb and YBCO superconductor core fibers with fused silica claddings have been demonstrated. Surface morphology, chemical composition, interface effect, and superconductivity were investigated to develop an understanding of the material-processing-performance relationships. The Pb core fiber surrounded with ordered holes was studied to determine the efficiency of cryogenic cooling by the surrounding holes. Theoretical calculations via a 1-D single-phase steady state model were also generated to evaluate the heat transfer mechanism.

The flow chart of the research process is shown in Figure 1.1.

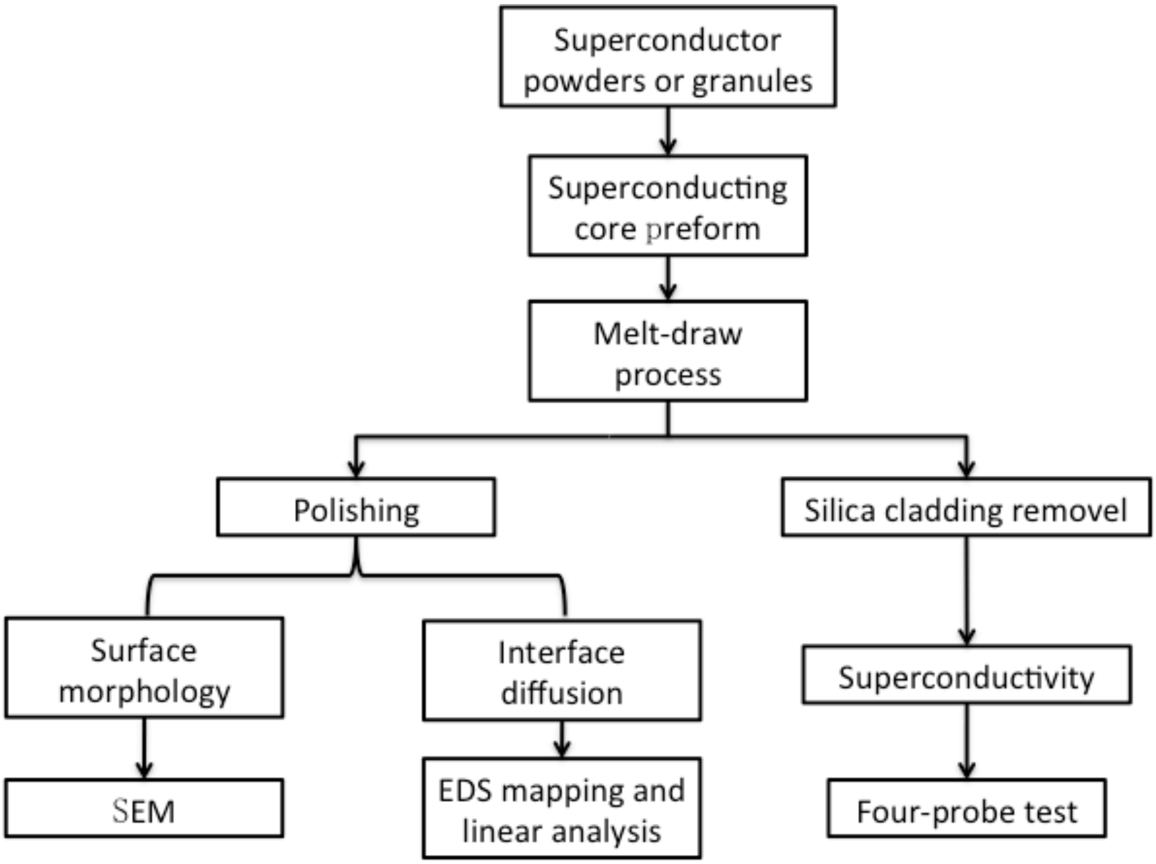

Figure 1.1 Flow chart of the process.

# 2 Background

## 2.1 History of superconductor materials

Superconductivity is a phenomenon of exactly zero electrical resistance and expulsion of magnetic fields occurring in certain materials when cooled below a critical temperature ($T_c$). The electrical resistivity of a metallic conductor decreases gradually as temperature is lowered. The decrease of resistance is limited by impurities and other defects in ordinary conductors, such as copper or silver that is typically used in electrical cables. Near absolute zero temperature, a real sample of a normal conductor still shows some resistance. However, the resistance drops to zero when a superconductor is cooled below its critical temperature[7]. The temperature dependence of resistance of a normal metal conductor and a superconductor is shown in Figure 2.1.

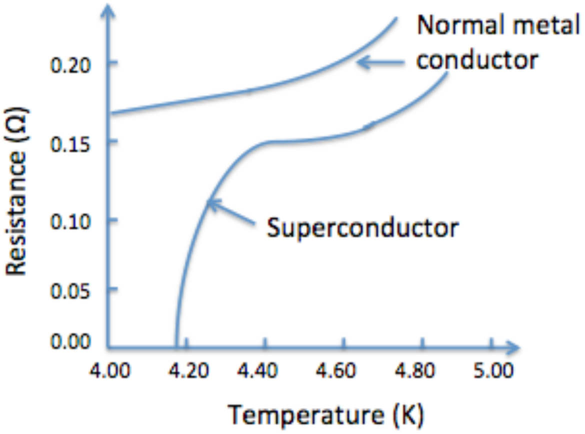

Figure 2.1 Temperature dependence of resistance of a normal metal conductor and a superconductor.

This discovery was first found by Kamerlingh Onnes and his colleagues of the Leiden University in the Netherlands In 1911 that the electrical resistance of mercury abruptly vanished at 4K [8]. Above 4.2 K, the resistance of mercury just gradually decreases. But just below 4.2 K, it soon disappears due to the superconductive property of the material[9].

Expelling all magnetic fields from its interior is the second important characteristic for the superconducting state and is often used to distinguish a conductor and a superconductor. This unusual magnetic expulsion phenomenon is known as the Meissner effect [10] (see Figure 2.2). A magnetic piece can be lifted by this effect and theoretically can remain in this position as long as the superconductor is under its critical temperature. Since these fantastic phenomena were found in the superconductor, it has appeared on the historical stage and currently plays an important role in super speed magnetically levitated trains [11, 12].

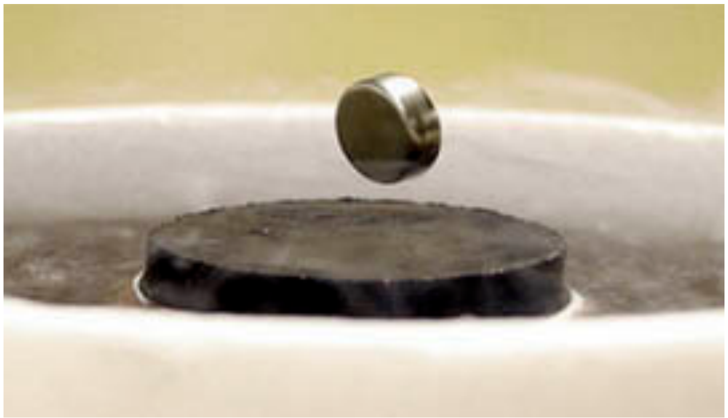

Figure 2.2 The Meissner effect of magnetic piece on the YBCO pellet in liquid nitrogen bath, photo by author, 2014.

Only after 2 years of Onnes' discovery, Pb was found to be superconductive at 7.2K. The highest critical temperature reported for simple metals was 9K for Nb in 1930. After then, it was expanded to carbides and nitrides, which raised the $T_c$ up to 23 K in 1973.

Figure 2.3 illustrates the historical development of superconducting materials related to $T_c$. The high temperature superconductor materials composed of $YBa_2Cu_3O_7$ (YBCO) were found in 1987 by Wu and Chu[13]. All materials developed before 1986 became superconducting only at temperatures near the boiling points of liquid helium ($T_b$ =4.2 K) or liquid hydrogen ($T_b$ = 20.28 K) : the highest being $Nb_3Ge$ at 23 K. The discovery of superconductivity in YBCO changed the world. It is the first known superconductor with $T_c$ above the boiling point of liquid nitrogen ($T_b$=77 K). The low cost of liquid nitrogen made the application of superconductivity plausible on a large scale. Subsequently, the search for much higher $T_c$ materials and research on superconductors returned to humans' eyes, with this temperature threshold (77 K) employed to differentiate between low $T_c$ and high $T_c$ superconductor (HTS).

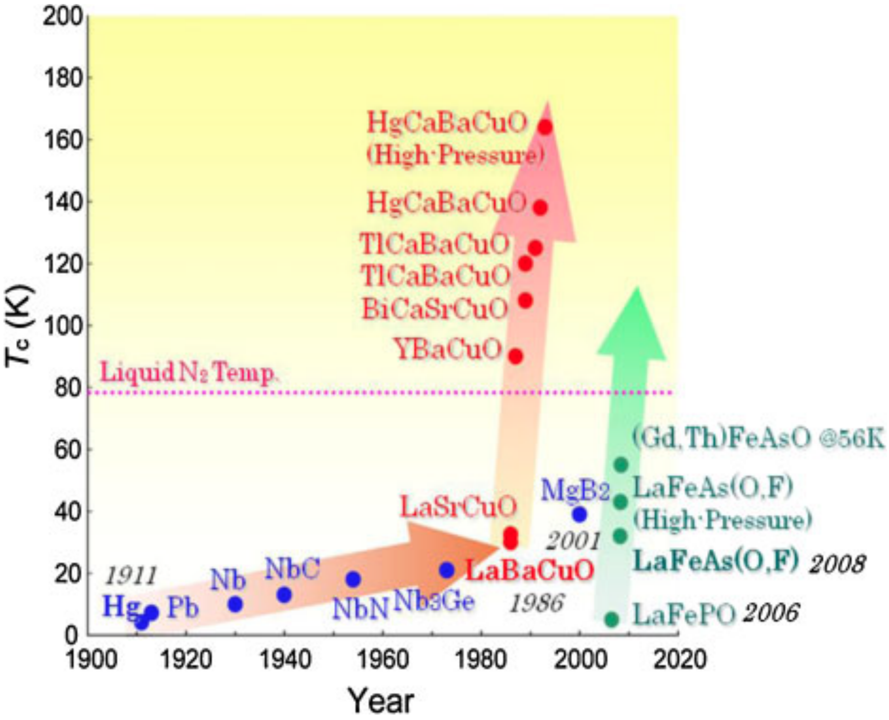

Figure 2.3 Developing trend of superconducting critical temperature over last 100 years[14], Reprinted from The Japan Society of Applied Physics, 51(1), K. Kitazawa, Superconductivity:100th Anniversary of Its Discovery and Its Future, Copyright(2012), with permission from The Japan Society of Applied Physics, All rights reserved..

$YBa_2Cu_3O_7$ is an oxygen-deficient triple perovskite (Figure 2.4a), where Y and Ba are the central A cations and Cu is the B cation. Oxygen is missing from the central Y layer and from the a-axis of the basal plane. Cu(1) is coordinated to four oxygens in a square planar configuration, corner-sharing to form chains along the b-axis. Cu(2) is square-pyramidally coordinated with the $CuO_5$ units corner-sharing to form buckled sheets in the a-b plane[15]. The oxygen stoichiometry of $YBa_2Cu_3O_x$ can vary over the range $6<x<7$[16] and properties range from superconducting ($6.5<x<7$) to semiconducting ($x<6.4$)[17, 18]. $YBa_2Cu_3O_7$ is orthorhombic, but as the oxygen content decreases, the structure undergoes a phase transition to tetragonal symmetry. Figure 2.4 shows the change in structure: in (a), for $x=7$, all the $O_{b1}$ sites are occupied, and $O_{b2}$ sites are empty. On removal of oxygen from $O_{b1}$, the $O_{b2}$ sites become partially occupied, until at (b) the orthorhombic-tetragonal (O/T) phase transition occurs when the $O_{b1}$ and $O_{b2}$ sites are equally occupied and (c) shows the structure of $YBa_2Cu_3O_6$ in which all the oxygens are missing from the basal plane.

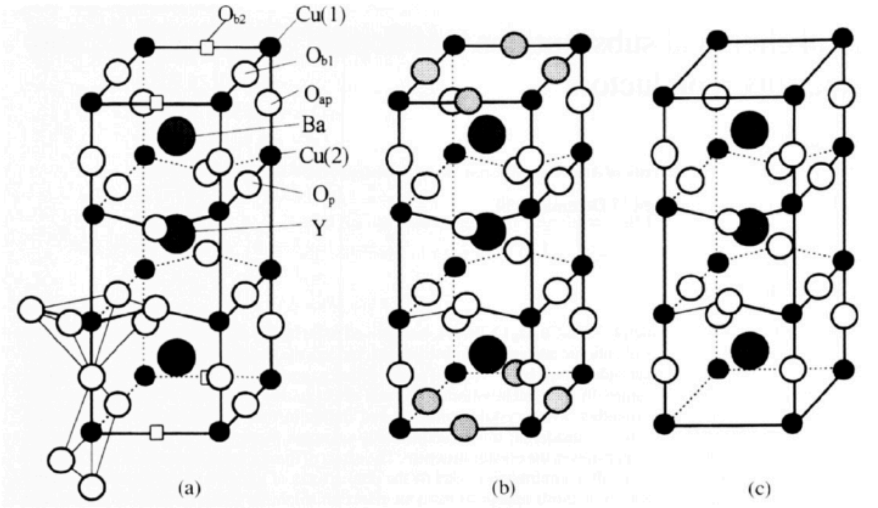

Figure 2.4 Crystal structures of $YBa_2Cu_3O_x$ according to different oxygen ratio: (a) $x=7.0$, squares represent vacancies, (b) $x=6.5$, light shaded circles represent half-occupied sites. (c) $x=6.0$[15], Reprinted from Materials Science & Engineering R-Reports, 23(1), J.M.S. Skakle, Crystal chemical substitutions and doping of $YBa_2Cu_3O_x$ and related superconductors, 1-40, Copyright(1998), with permission from Elsevier, All rights reserved..

The critical temperature, $T_c$, is strongly dependent on oxygen content. $T_c$ remains approximately constant at ~90 K for $6.8<x<7.0$ and drops to another plateau at 60 K for $6.5<x<6.7$[19-22]. The absolute oxygen content is crucial to superconductivity, as well as the oxygen ordering.

According to BCS theory, the following are required to achieve a high critical temperature[14]: (1) a crystal lattice with a high vibration frequency, (2) strong interaction between electrons and the lattice, and (3) a high electron density of states on the Fermi surface. As the understanding of superconductivity in materials improves and other materials are discovered, the number of potential applications will increase. Thus, simple and cost effective superconductive conductor designs and fabrication processes are required to enable wide implementation.

The high $T_c$ superconductor compounds were extensively investigated in recent years. The critical temperature of 117 K was discovered in $Bi_2Sr_2Ca_2Cu_3O_{10}$ in 1988[23]. More exciting, a Fe-based superconductor (LaFeAsO) was also discovered by Hosono and his colleagues of Tokyo Institute of Technology in 2008 [24]. The critical temperature of the superconductor was found at around 135 K in $HgBa_2Ca_2Cu_3O_8$ [25]. It was also demonstrated that under high pressure, the critical temperature can be as high as 164 K [26].

With more and more superconductors being discovered, people found that superconductor materials could be divided into type I or type II depending on the transition characterization. For type I superconductors, full Meissner flux expulsion is exhibited before the transition to the normal state. For type II superconductors, a second superconducting phase that allows the magnetic field to penetrate the superconductor in small normal state pockets without general breakdown of superconductivity. The London penetration depth, $\lambda$, is used for the characteristic length of the distance that a magnetic field penetrates into a superconductor. Most of the pure element superconductors tend to be type I. Type-II superconductors are usually made of metal alloys or complex oxide ceramics. All high temperature superconductors are type-II superconductors.

The practical application of superconductivity technologies developed slowly due to the low critical temperature and the high cost that is required to cool them. The ultimate goal of ongoing superconductor research remains to be the development of a room-temperature superconductor material, as well as to find cost effective approach to realize wide implementation of the current high temperature superconductors.

## 2.2 Promising for superconductor optical fiber on ultralow noise light detector and sensing

After the first time discovery of superconductivity in 1911, little progress was made to clarify the mechanism of it or its practical application over the next 50 years. The demonstration of superconductivity in HTS materials prompted the identification of many promising applications. The applications of superconductors rely on the properties: persistent current, perfect diamagnetism (the exclusion of magnetic flux from superconductors), and the Josephson effect (the macroscopic interference of electron waves). The zero resistance has been used in power transmission networks[27]; the Meissner effect has been widely used in superconducting magnetically levitated trains; the Josephson effect has important applications in quantum-mechanical circuits, such as SQUIDs, superconducting quantum computing, and RSFQ digital electronics[28]. Figure 2.5 shows the industrial application of superconducting power and magnetic technologies.

Recently, superconducting devices have also found applications in fast and ultra-sensitive optical detection, because of their picosecond range relaxation times, repetition rates in the GHz range, low-noise background, and high radiation hardness[29]. The discovery of HTS by Bednorz and Muller in 1986 evoked proposals for making IR photon detectors in HTS[30]. The femtosecond photoconductive and electro-optic measurement techniques exhibit a 1 THz bandwidth and sub-millivolt amplitude sensitivity and enable the direct determination of intrinsic thermalization and relaxation times. Experimental results have been reported on the photoresponse of various HTS detector structures [31-33]. In the next section a review of the fundamental theoretical mechanism of photoresponse of superconductor and its practical applications and assumption in optics is presented.

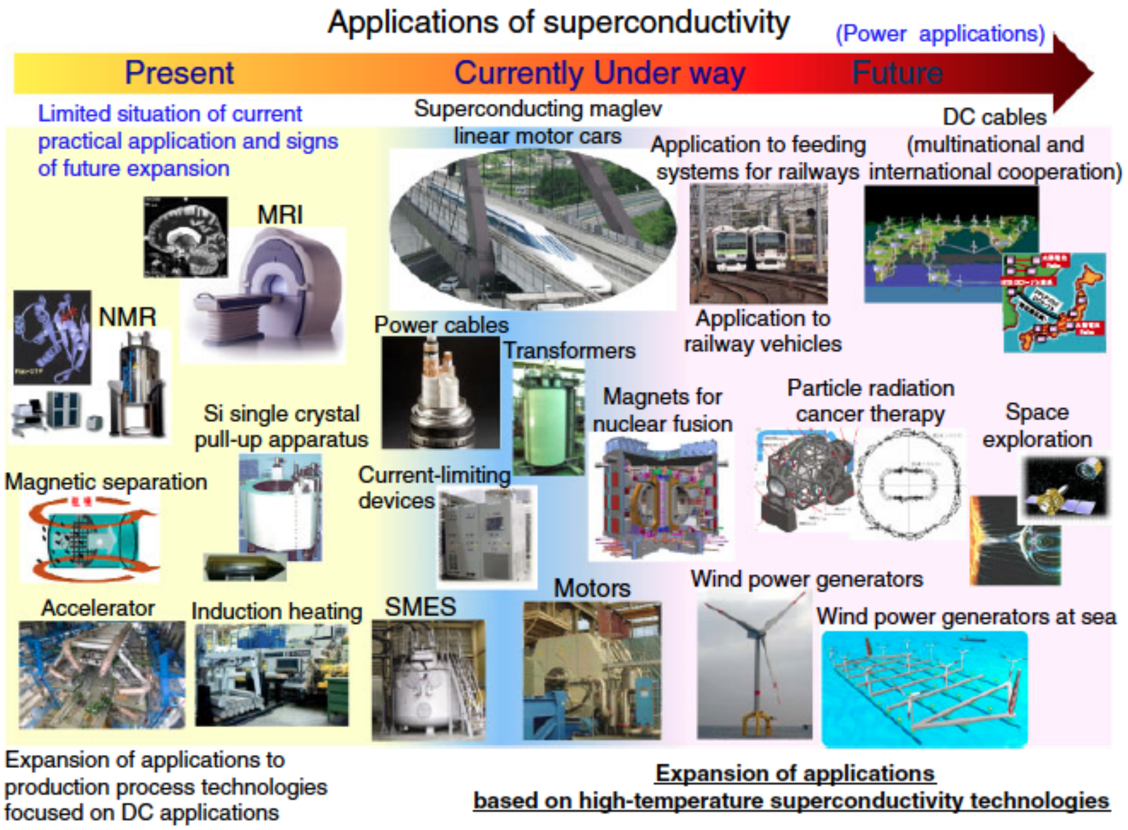

Figure 2.5 Main applications of superconducting power and magnetic technologies[14], Reprinted from The Japan Society of Applied Physics, 51(1), K. Kitazawa, Superconductivity:100th anniversary of its discovery and its future, Copyright(2012), with permission from The Japan Society of Applied Physics, All rights reserved..

### 2.2.1 Photoresponse for superconductor

In superconductors, two electrons pair up and produce a bound state by means of an attractive potential field defined as Cooper pairs. When these Cooper pairs break apart, they form negatively charged electrons and positively charged holes; the unpaired electrons are called quasiparticles. The energy for breaking these Copper pairs needs to be larger than its binding energy, denoted by 2Δ (where Δ is the energy gap on the order of meV). The small value of the Δ provides the production of an avalanche of excited quasiparticles in the superconductor, even after the absorption of a single optical photon[34]. The photoresponse dynamics of the perturbed superconductor and its recovery into the equilibrium state depend on various scattering processes, involving phonons, and Cooper pairs.

The basic requirements for a superconducting quantum detector are as follows[35, 36]:

(1) Quantum excitations to create excess quasiparticles by breaking Cooper pairs with photons that have energy greater than 2Δ;

(2) Efficient detection of the excess quasiparticles by measuring a property sensitive to the condensate population.

The theoretical predictions indicated that high temperature superconducting detectors could be realized [37]. According to BSC theory, the value of 2Δ is given by 3.53 meV. For a transition temperature of 90 K (typical for YBCO), the energy gap predicted by this relation is 27 meV [38].

The density of quasiparticles in a superconductor is given by[39] :

$$n_t = 2N_0(\pi E_g kT)^{1/2} \exp\left(-\frac{E_g}{2kT}\right) \qquad (1)$$

where $N_0$ is the single spin density of states at the Fermi level at T=0.

The analysis of the recombination lifetime in superconductors indicates a dominant contribution by the electron-phonon interactions. Rothwarth and Taylor showed that the effective quasiparticle lifetime can be approximated by the following equation[40]:

$$\tau_{eff} = \frac{\beta n_t t}{8N_{\omega t} s} \qquad (2)$$

where $N_{\omega t}$ is the equilibrium density of phonons with the energy $h\omega/2\pi > 2\Delta$, s is the velocity of sound ($\approx 3\times10^2$ m/s) and $\beta > 1$. Assuming that the device thickness is in the range of 20-100 nm, the thermal generation rate of quasiparticles is [41]

$$G_{th} = 4\times10^{41}\frac{TE_g^2}{\beta s^2}\exp\left(-\frac{qE_g}{kT}\right) \qquad (3)$$

Figure 2.6 provides the intrinsic photo response of a YBCO superconductor, with the positive 0.86 ps wide part representing the process of Cooper pair breaking and the negative part corresponding to the pair recombination. From this point of view, superconductors are preferable for digital and communication applications due to this ultrafast response.

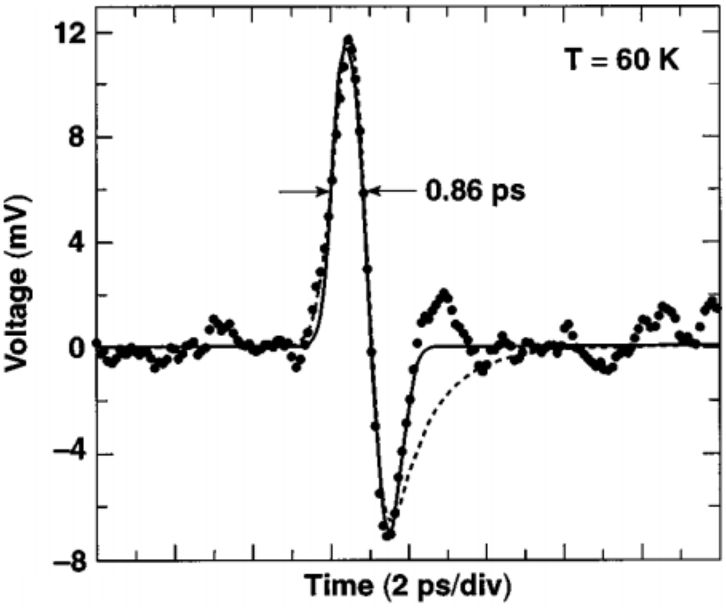

Figure 2.6 Measured voltage transient (dots) and the fitted nonequilibrium kinetic-inductive responses models, when the bridge was biased in the superconducting state[33], Reprinted from Applied Physics Letters , 74(6), M. Lindgren, Intrinsic picosecond response times of Y-Ba-Cu-O superconducting photodetectors, 853-855, Copyright(1999), with permission from Copyright Clearance Center, All rights reserved.

### 2.2.2 Superconductor for photodetector applications

Superconducting devices have been further developed for ultra-low-noise detection of telecommunication band photons in recent years. Relatively lower detection efficiencies, lower than 5% in some devices, has been demonstrated on NbN-based superconducting single photon detectors, which can be operated at 4 K temperature with detection rates approaching a gigahertz [42, 43]. The single photon detector is designed as a meander-shaped nanoscale wire and shows current biased slightly below its critical current. A hotspot can be formed in the wire by the energy of an absorbed photon. The detection mechanism can be described as the momentary breakage of the superconductivity causing a transient voltage in the external circuit.

In order to realize ultra fast and low loss detection devices, the traveling wave photodetection strategy has been taken to integrate optical waveguides and superconductive structures[6]. Figure 2.7 illustrates the physical structure of a YBCO superconducting optical waveguide with a yttria-stabilized zirconia (YSZ) buffer layer using $SiO_2$ as the low-index interlayer. This design can be used for multichip interconnections[6, 44]. The appropriate thickness of the YSZ layer should be chosen such that thicker layer results in a low-loss waveguide[6].

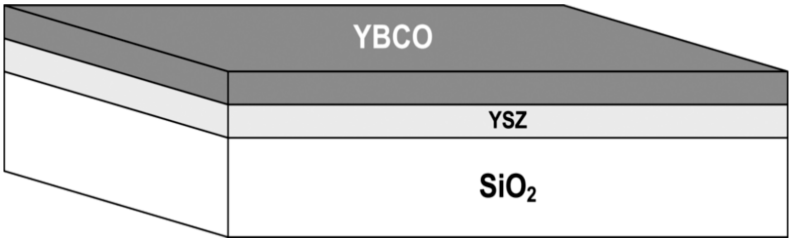

Figure 2.7 The schematic of a superconducting optical waveguide[45], Reprinted from Ieee Transactions on Applied Superconductivity, 18(4), B.G. Ghamsari, Theory of superconductive travling-Wave photodetectors, 1761-1768, Copyright(2008), , with permission from Copyright Clearance Center, All rights reserved.

## 2.3 Superconductor fiber fabrication

The fiber optic revolution in telecommunication and sensing applications was, in part, facilitated by economically robust designs and manufacturing processes [46]. Several variations of the chemical vapor deposition and drawing processes are proven technologies that have matured to a level of worldwide acceptance[47]. Recently, it has been demonstrated that these synthesis routes can be readily adapted to other materials such as metals, semiconductors, ceramics etc[48-52]. Traditional optical fiber manufacturing may provide a cost effective and efficient way for superconductor core fibers.

### 2.3.1 Bulk melt for superconductor

Figure 2.8 Photograph of a large Y-123 single crystal (30 mm diameter and 12 mm height) [53], Reprinted from Superconductor Science & Technology, 35(7), Babu, N.H., Growth of large sized $YBa_2Cu_3O_7$ single crystals using the top seeded melt growth process, Copyright(2012), with permission of IOP Publishing. All rights reserved.

The melt processing technique has been developed for fabrication of large grain superconductors. A pre-sintered green body of the desired composition can be rapidly heated to a temperature well above the melting temperature. Formation of the superconductor phase is achieved by the controlled cooling procedure. Melt processing techniques including directional solidification processes help in achieving high density, and highly orientated structure superconductors[10]. Figure 2.8 shows a Y-123 single crystal prepared by a top seeded melt growth process. It contains a continuous, superconducting single crystal phase matrix.

The bulk melt process was also attempted to produce superconductor wire. The superconductor rod pressed by fine powder can be rapidly heated to about 1200-1300 °C and melted in air. The wire was obtained by pulling the melt part before solidification. The product quality depends on controlled temperature, time, and mechanical motion[54].

### 2.3.2 Superconductor wire fabrication

The powder-in-tube (PIT) technique, among various methods to produce metal/superconductor composites, has proved to be an attractive route for producing superconducting wires[55-57]. The success of the PIT process to realize a small filament diameter, the possibility to draw wires without intermediate heat treatments, the short reaction heat treatment, and the clear potential for further optimizations[58].

The PIT processing steps are shown schematically in Figure 2.9. It is often used for electrical conductors from brittle superconducting materials, such as $Nb_3Sn$[59], $MgB_2$[60], iron based superconductors[61].

At this time, high temperature superconductors are too brittle for normal wire forming processes, so the tubes are often metal, like silver. They are heated to react the mix of powders and then can be flattened to form a tape or wire-like conductor. While, for most of ceramic superconductors such as YBCO [62], PIT technique usually can make ribbon-shaped and large size wire but lacks the ability of preparing different shapes and much smaller size wire.

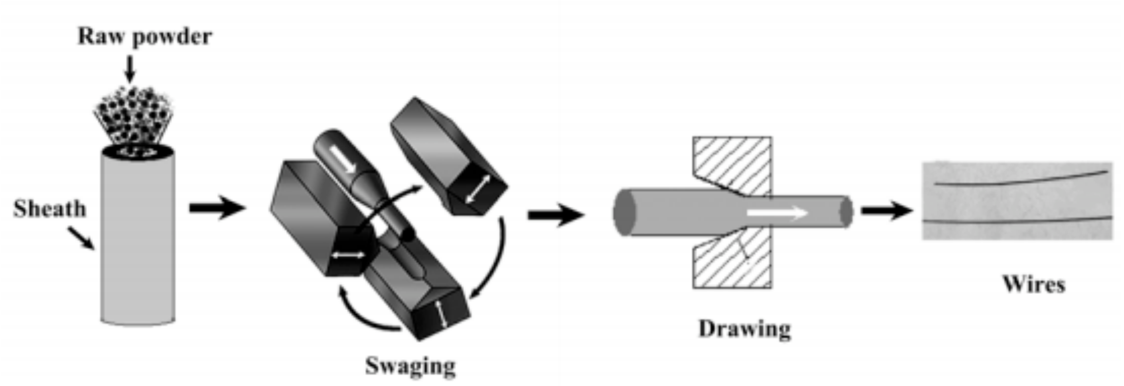

Figure 2.9. Schematic view of the deformation steps for the fabrication of an iron pnictide wire by the PIT technique[61], Reprinted from Physica C-Superconductivity and Its Applications, 469(9-12), Y.W. Ma, Fabrication and characterization of iron pnictide wires and bulk materials through the powder-in-tube method, 651-656, Copyright(2009), with permission from Copyright Clearance Center. All rights reserved.

### 2.3.3 Optical fiber fabrication

The traditional fiber preparation technique includes preform preparation and fiber drawing. The preform for fiber-drawing normally is prepared by direct-melt method or vapor-phase oxidation process[63]. In the vapor-phase oxidation process, a material is made to react in a vapor phase and is then deposited. Since the vapor pressure differs from substance to substance, when a liquid material is vaporized at a nearly fixed temperature, impurities in the liquid can be left un-vaporized and only the desired substance can be vaporized. Therefore, the purity of the material becomes much higher in the vapor phase than in the liquid phase: sufficiently high to make it usable for fiber making. If a material is properly chosen, the vaporizing temperature need not be kept so strictly constant and vaporization can be controlled relatively easily[10].

Vapor-phase oxidation process has developed into four different branches, outside vapor-phase oxidation (OVPO)[64], vaper-phase axial deposition (VAD)[65], modified chemical vapor deposition (MCVD)[66], plasma-activated chemical vapor deposition (PCVD)[67]. The vapor-phase oxidation process is preferable to realize high purity optical fiber.

The direct draw method can be more convenient and economical. The preform is heated in the furnace and is drawn into the fiber. The softening temperature of fused silica is approximately 1650 °C[68]. Fiber drawing is performed at approximately 2000 to 2100 °C. The drawn fiber must have a sufficient mechanical strength to withstand practical use, and the fiber diameter must be uniform.

The schematic of an optical fiber drawing process is as shown in Figure 2.10. According to the heating regions, it can be divided into heating zone, natural cooling zone. The glass preform is heated in the furnace.

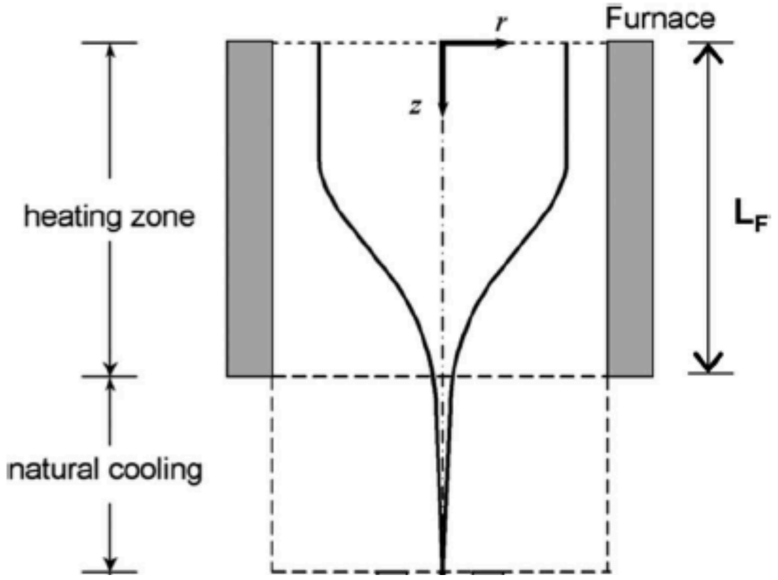

Figure 2.10 Schematic of an optical fiber drawing process showing the neck-down region in the furnace[69], Reprinted from Ieee Photonics Journal, 2(4), A. Mawardi, Optical fiber drawing process model using an analytical neck-down profile, 620-629, Copyright(2012), with permission from Copyright Clearance Center. All rights reserved.

During the fiber drawing process, the heating temperature, heating zone height, the size of preform and the drawing speed of the fiber all affect the final fiber prepared. So it is very critical to manufacture the uniform fiber with all of the required parameters controlled.

# 3 Materials and Experimental Procedure

## 3.1 Superconductor core fiber fabrication

### 3.1.1 YBCO powder press

Figure 3.1 shows the schematic of hydraulic press. The pressing die used was for 1/4 inch I.D. core sample. The lower level was sealed with lower punch of the pressing die and then put the YBCO powders inside the pressing die. The upper punch was slightly pushed into the pressing die. Then, two sides of support plate were used to hold the pressing die during pressing. The pressing die was pressed up to 3 metric T under the hydraulic force for ten minutes. The sample was obtained after demolding. The sample was around 1/4 inch diameter rod.

Figure 3.1 Schematic of hydraulic press, photo by author, 2014.

### 3.1.2 Preform manufacture

A fiber drawing system is custom designed for drawing fibers from a preform. To date, all the fibers were fabricated on a glass-working lathe, Litton Model HSJ143. The schematic of the instrument is shown in Figure 3.2. The system has two chucks that clamp both ends of the preform. One of the chucks is attached on a motorized linear stage. The traversing tailstock chuck can be moved backwards so that the fiber can be obtained. Subsequently, the maximum achievable fiber lengths are limited by the working distance, between the chuck faces, as well as the preform length, and drawing rod at the tailstock end.

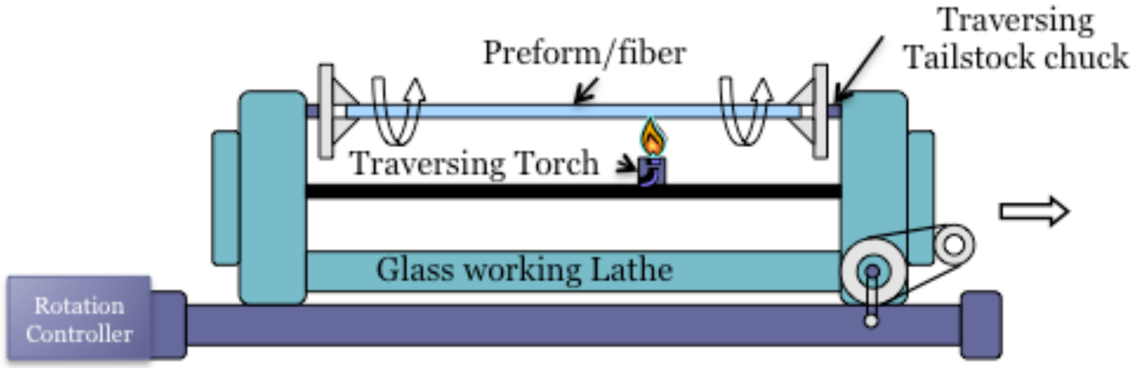

Figure 3.2 Glass processing lathe

The superconductor core fibers were fabricated into a two-part structure, a fused silica cladding surrounding and a solid superconductor core. The fiber preparation began with construction of a preform from which the fibers were pulled. A fused silica substrate tube (GE214, OD=8 mm, ID=3 mm) was fused to a processing tube (GE214, OD=9.5 mm, ID=7 mm).

Figure 3.3 details the beginning process to prepare the preform. The bulk superconductor materials were placed into the processing tube and melted via an oxy-hydrogen flame at a temperature of approximately 600-800 °C for Pb and 1300-1500 °C for YBCO (a little above melting temperature of superconductor). When the superconductor materials inside the tube were melted, a smaller diameter fused silica rod (GE214, 6 mm) was used to push the superconductor melts into the substrate tube forming a preform with a superconductor core.

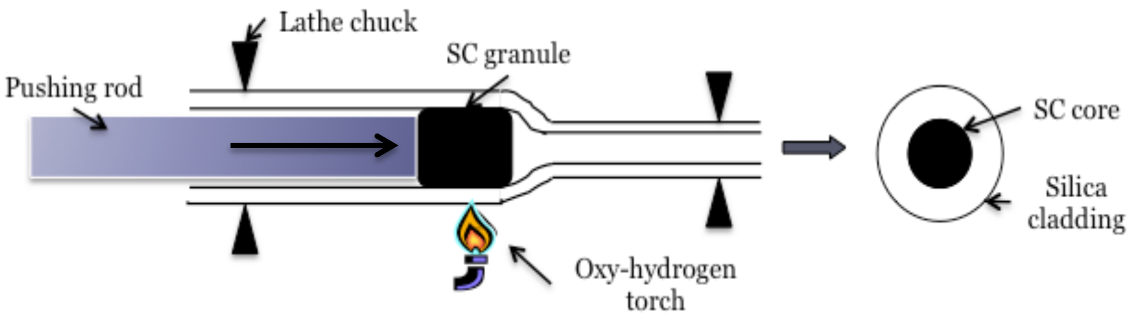

Figure 3.3 Superconductor core fiber preform manufacture flow chart

### 3.1.3 Fiber-drawing

For the fiber drawing process, the superconductor based preform was secured with both ends attached to glass lathe chucks. The oxy-hydrogen torch was used to heat the preform to a temperature higher than 2000 °C based on the glass viscosity observed during the fiber draw, as shown in Figure 3.4.

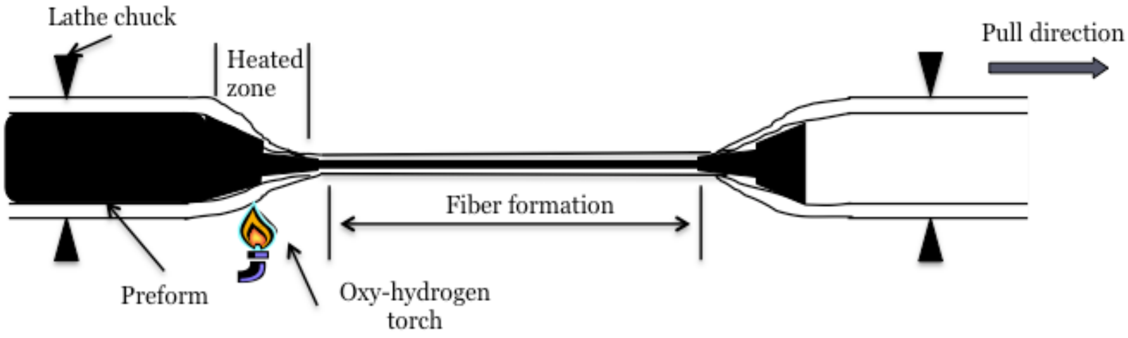

Figure 3.4 Superconductor core fiber drawing flow chart

When the superconductor core was molten and the silica tube was sufficiently softened, the secondary chuck was moved in the linear direction to draw a fiber from the preform. Fiber diameters in the range of 100-1000 μm were routinely fabricated.

### 3.1.4 Ordered hole fiber-drawing

The ordered hole Pb core fiber was fabricated using a similar process as described in the previous section, but included several fused silica tubes displaced around a “core” fused silica tube containing the Pb materials. First, a fused silica substrate tube (GE214, OD=6 mm, ID=3 mm) was fused to the “core” tube (GE214, OD=12.75 mm, ID=10.5mm). Pb granules (Alfa Aesar, approximately 3mm, 99.9% (metals basis)) were placed in the processing tube. The “core” tube was then inserted and centered in an overclad tube (GE214, OD=12.75mm, ID=10.5mm). Smaller fused silica tubes (GE214, OD=3mm, ID=1mm), were then displaced around the “core” tube in the annulus between the overclad tube. A section of this preform was then heated to approximate 2000°C to allow the overclad tube to “naturally” collapse on the small tubes. As the Pb melted, this structure was drawn into a fiber.

## 3.2 YBCO heat treatment

During the melt-draw process, the YBCO core decomposed easily. Further heat treatment was needed to recover the superconductive state. Oxygen flowing through the tube furnace was needed during YBCO core heat treatment.

Under the following heat treatment procedure, the superconductive YBCO was achieved: heat YBCO fiber to 950 ˚C and hold for 12 hours at 5 ˚C/min, then decrease to 500 ˚C at 1 ˚C/min and hold for 12 hours of annealing and then cool to room temperature (all the procedures involving $O_2$ flowing through the tube furnace at the rate of 0.2 sL/min). The schematic of tube furnace setup is shown in Figure 3.5.

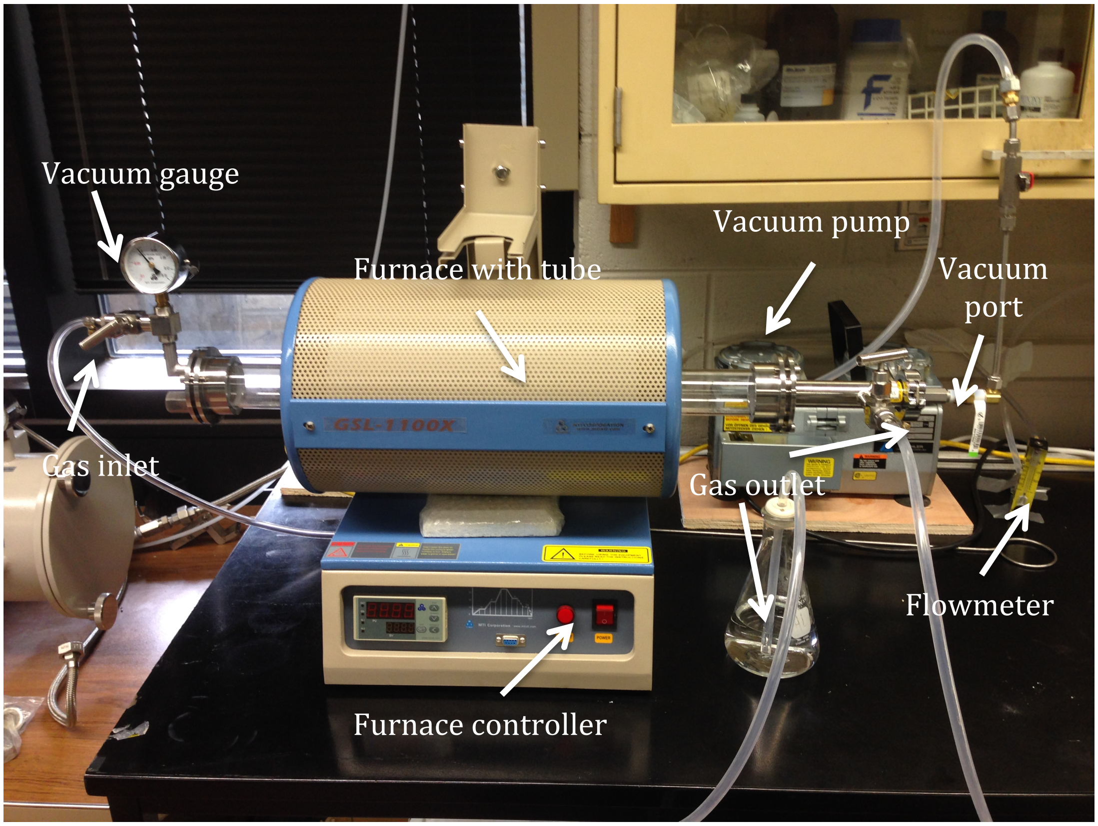

Figure 3.5 Schematic of tube furnace setup, photo by author, 2014.

## 3.3 Sample polishing

Select fiber samples were examined on the polished surfaces. The polishing system used is shown as Figure 3.6. The superconductor core fiber was secured on the sample holder to keep it vertical to the polish paper. The water supply was used to wash out the scrap during polishing. The rotation speed was controlled around 90 rpm. The fine diamond polish paper (Angstrom Lap) from 30 μm down to 0.2 μm was used to get the fiber surface flat and smooth. During polishing, the surface was periodically checked under optical microscope.

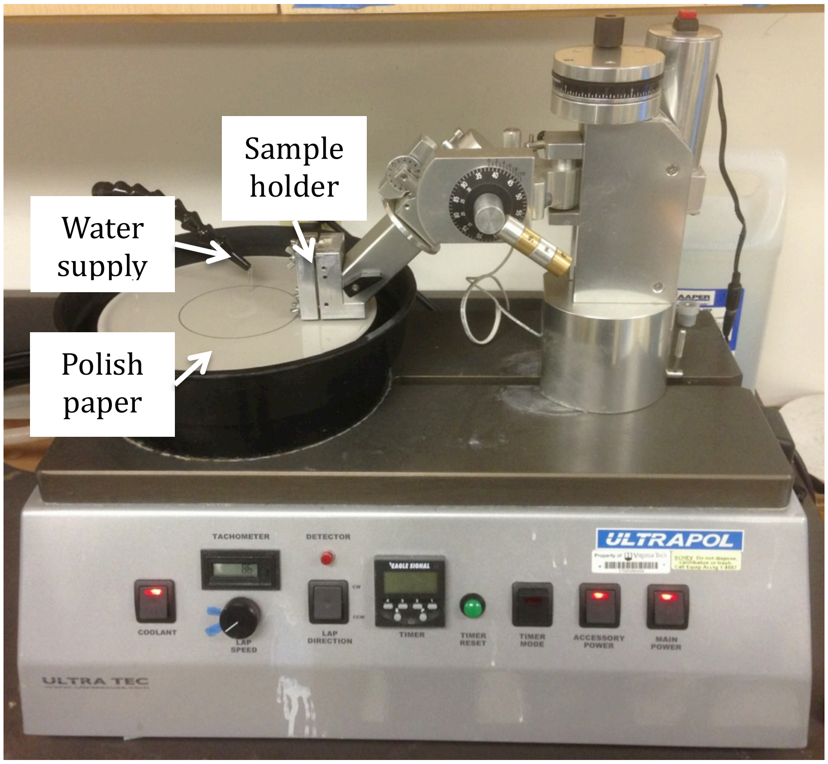

Figure 3.6 Superconductor core fiber polishing equipment, photo by author, 2014.

## 3.4 Characterization

### 3.4.1 SEM/EDS mapping

An environmental scanning electron microscope (ESEM, FEI Quanta 600 FEG) was used with accelerating voltage set to 5-30.0 kV. Scanning electron microscopy was used in order to obtain micrographs of the superconductor core fiber microstructure. Energy dispersive spectroscopy (EDS, Bruker QUANTAX 400) chemical composition and mapping were performed with a high speed silicon drift detector. The analysis was conducted on samples sputter coated with gold/palladium for about 40 s using the Cressington High Resolution Sputter Coater 208 HR in order to reduce effects caused due to charging of the sample by providing a conducting path for the electron transfer.

### 3.4.2 Superconductivity of the Pb superconductor core

The resistance versus temperature measurement is usually used for determination of superconductor materials. Two-probe causes error when measuring low resistance due to contact resistance of measuring leads. So four-point test is used for testing the superconductivity of superconductor materials.

The test setup is shown schematically in Figure 3.7. A constant current ($I_{14}$) (HP Hewlett Packard Agilent, 6633A System DC Power Supply) was used to flow the length of the sample through two probes labeled 1 and 4. The voltage ($V_{23}$) was measured between two center probes labeled 2 and 3 via a voltmeter (HP Agilent, 34405A, 5 1/2 Digit Multimeter). The high input impedance of the voltmeter minimizes the current flow through it. Then the potential drop across the contact resistance associated with probes 2 and 3 is negligible[70]. Therefore, the resistance of the sample between probes 2 and 3 is the ratio of the voltage drop $V_{23}$ to the current $I_{14}$. Labview software was used to record the data of voltage and temperature simultaneously.

The parameters chosen in this research is critical since several rules must be considered as below:

(1)-The current should be chosen well below the critical current of the superconductor;

(2)-The current used should avoid the sample heating.

In all tests, the voltage drop across the voltage probes was held constant at approximately 1-1.1 mV at room temperature. The following equation is utilized to determine the required current:

$$R = \frac{V}{I} \tag{4}$$

(R: resistance; V: voltage; I: current)

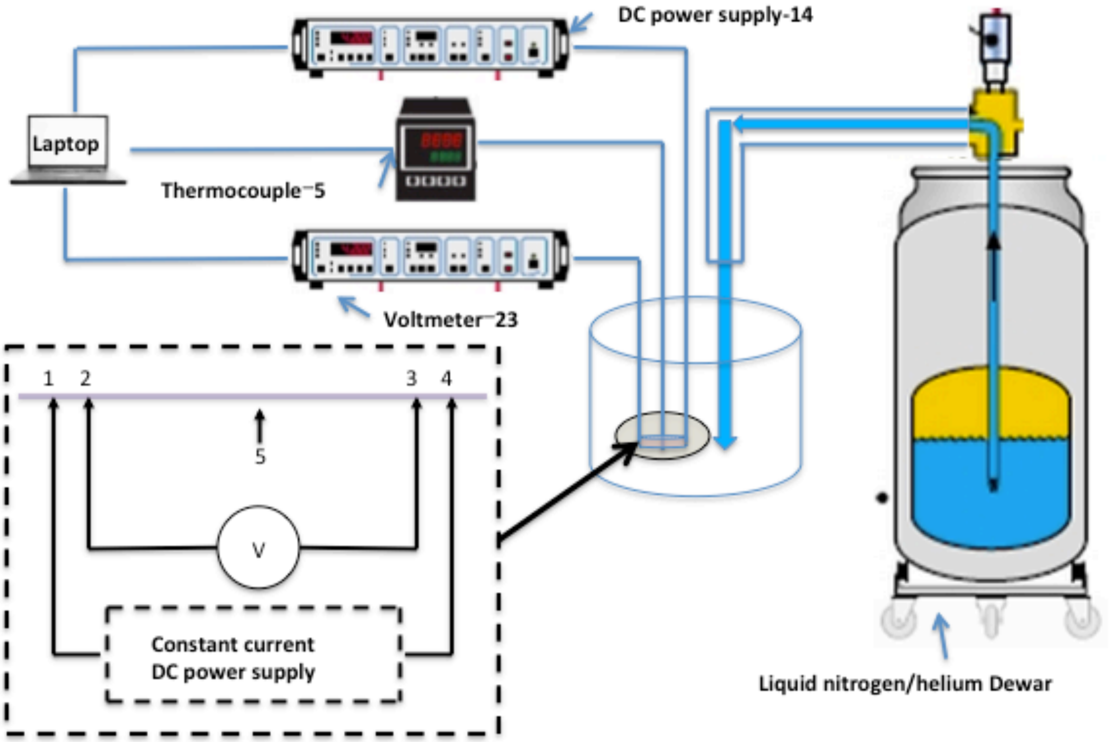

Figure 3.7 Schematic of a four-point method.

Since the Pb core had a smaller cross sectional area than the Pb wire, the resistance was larger. Thus, a smaller current was required for the Pb core to produce the same room temperature voltage drop of approximately 1-1.1 mV.

Before the test for our samples, the commercial laminated brass YBCO wire (Tc around 90 K) was used to validate the four-probe test setup. It was shown in Figure 3.8. The critical temperature of commercial YBCO was shown to be around 92 K, which is close the real Tc of this material. This procedure confirmed the capability of our setup.

During the four-probe test, the smaller diameter fiber showed poor contact with the conductive lead and also was easy to break apart. The diameter of the Pb core was around 0.8-1 mm and the length of fiber was around 50 mm. The Pb core with silica cladding, the Pb core removed silica cladding and commercial Pb wires were tested for comparison. The liquid helium (boiling temperature= 4 K) was used because superconductivity of the Pb is around 7 K.

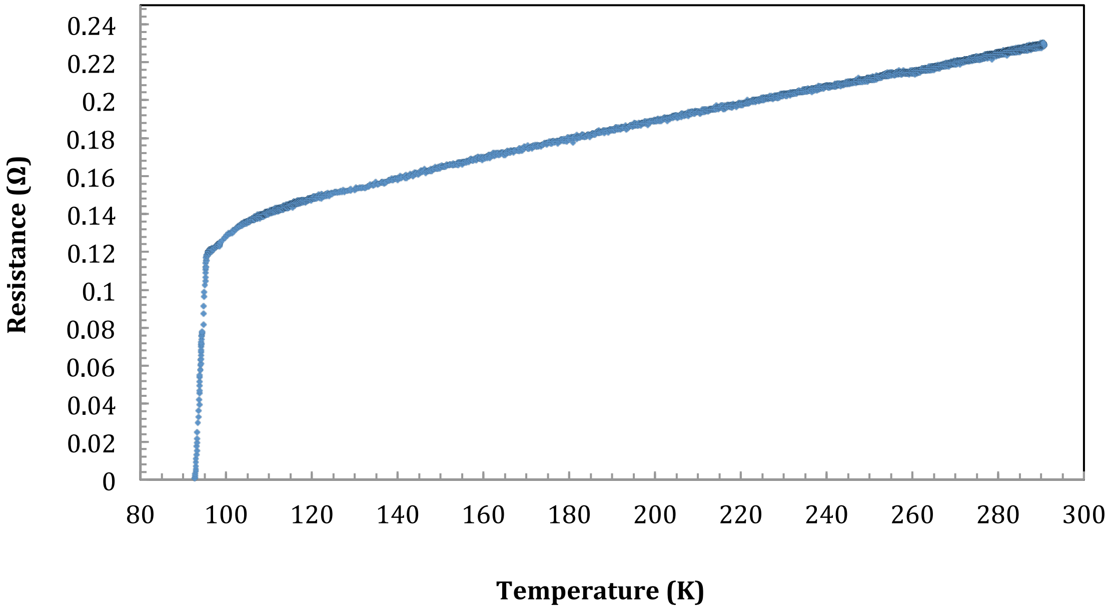

Figure 3.8 Commercial superconductor brass laminated wire.

### 3.4.3 Superconductivity of the YBCO superconductor core

Since the YBCO material is brittle, it was difficult to remove the glass cladding easily compared to the Pb core fiber. So the YBCO core fiber was mounted in epoxy resin. The sample was polished until the cross-section of the YBCO core was exposed. In order to get a larger contact area, the diameter of the YBCO core was fabricated around 0.8-1 mm.

The setup of the four-probe was also revised for the YBCO core fiber superconductivity test. The schematic of this setup is shown below:

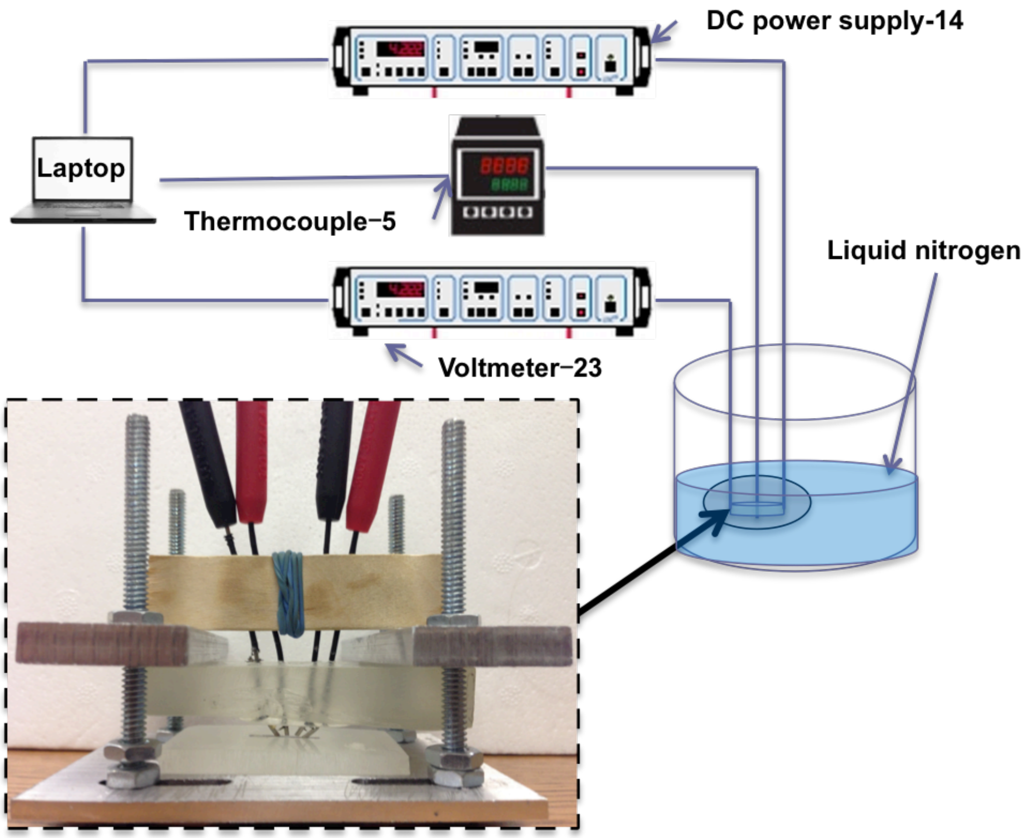

Figure 3.9 Schematic of setup for superconductivity of the YBCO core fiber.

The four-probes were first mounted in the epoxy mold with a spacing around 2.5 mm. The polished YBCO core fiber was put on the bottom of the holder plate. Then the four-probes were vertically pushed onto the surface of the YBCO core area. Four screws were used to form the press on the topside of the four-probe to make the setup mechanically stable. These four top screws adjust the contact force.

### 3.4.4 Efficient cooling of superconductivity of porous core cladding

The basic four point probe test setup was modified to verify the superconductivity of the Pb core upon liquid helium cooling via the holes in the fiber, as seen in Figure 3.10.

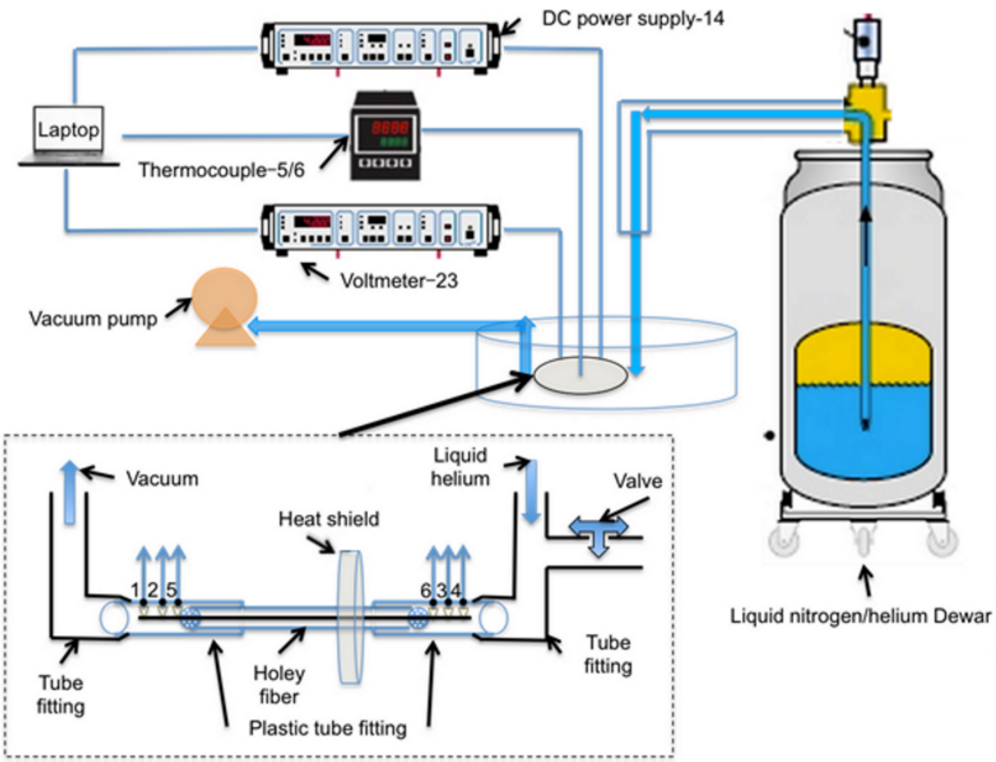

Figure 3.10 Modified four probe test setup for efficient cooling of porous cladding.

To assure accurate measurements and demonstrate basic feasibility, a sample with a fiber diameter of approximately 2000 μm and length of 64 mm was used for testing. First, the fused silica cladding was removed from both ends of the fiber to expose the Pb core. The outside diameter of the fiber was sealed to an intermediate plastic tube. Holes were made in the tube to allow for the probe connections and thermocouple measurements. In turn, epoxy was used to seal the holes in an attempt to minimize any liquid helium leakage. The intermediate tube was then connected to the helium transfer tubing. A three-way "safety" valve was placed in-line to avoid over-pressurization. Furthermore, the "outlet" end was connected to a vacuum to remove any residual air and assist the flow of liquid helium through the voids in the fiber. A composite alumina fiber insulation/plastic "heat shield" was positioned between the inlet end and the fiber length to assure that the sample was not cooled by extraneous liquid helium; no liquid helium migrated beyond the “heat shield”. It must be noted that the test fiber was not further insulated or coated.

Once set-up, the outlet valve of the commercial liquid helium dewar was opened to allow the gaseous helium and then liquid helium to flow into the tubing. The in-line safety valve was then slowly opened to assure all the liquid helium flowed to the sample. It was found that if the system was not sealed adequately, not enough liquid helium was allowed to infiltrate the pores of the fiber (this will be discussed in the next section). The voltage drop, current, and temperature measurements at both ends of the sample were continuously monitored during the test.

### 3.4.5 Experimental verification of the liquid nitrogen cooling

In order to simplify the process, liquid nitrogen was used since it is easily obtainable. Temperature is the key point to the measurement. The system must be sealed since leakage will break the suction capability.

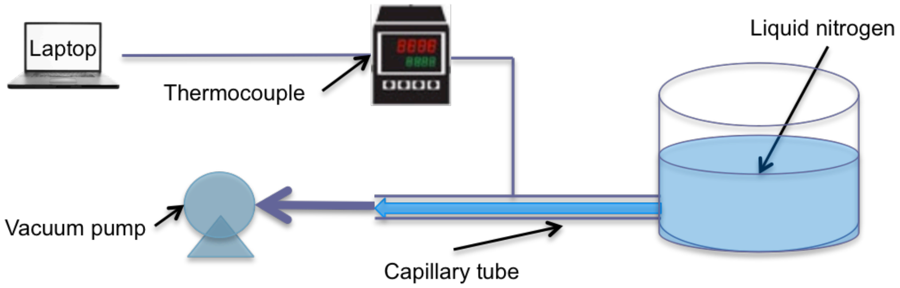

Figure 3.11. Setup of capillary tube cooling by liquid nitrogen.

Figure 3.11 shows the setup of capillary tube cooling by liquid nitrogen. The capillary tube was placed in a horizontal position to avoid the effect of gravity. The thermocouple was placed and bonded to the outside of the capillary tube at a specific position. A vacuum pump was used to suck the liquid nitrogen into the capillary tube and the temperature was monitored. The measured temperature and the length were used for comparison of the experiment results and the model calculations.

# 4 Pb Superconducting Core Fiber

## 4.1 Fiber fabrication

Pb melts at around 300 °C, and it flows smoothly in the silica tube when preparing the Pb core preform. Careful processing and appropriate thickness of the silica cladding were necessary since Pb could boil at the fiber draw temperature. Figure 4.1 shows the photograph of a Pb core fiber. The fiber around 45 cm (~18 inch) has been obtained. The overall diameters ranging from 200-900 μm and core diameters of 100-800 μm of the Pb core fiber could also be fabricated under controlled condition.

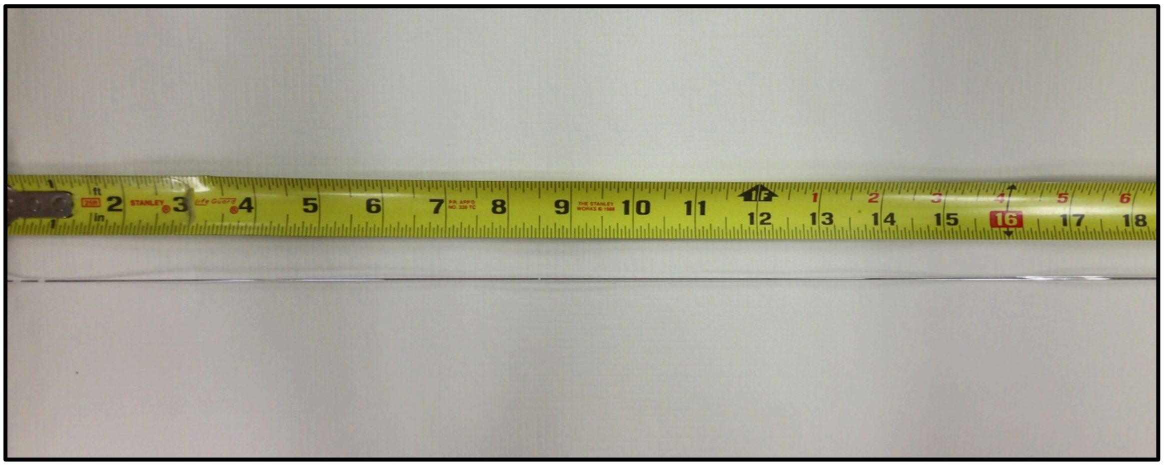

Figure 4.1 Photograph of a Pb core fiber, photo by author, 2014.

## 4.2 Surface morphology

The Pb core fiber was successfully prepared via the melt-draw technique. An SEM image of the cross section of the Pb core fiber is shown in Figure 4.2. The core is circular in cross section and there is a strong contrast between the Pb core and the fused silica glass cladding. Further, the interface is well defined and does not show signs of bubbles resulting from the melting of the core during fiber draw. The fused silica cladding maintained a diameter of approximately 430 μm and the Pb core diameter of 165 μm, respectively. There is some impurity particles located on the core-clad interface area with larger contrast compared to the Pb core. It is believed that the impurities are C brought by the polishing procedure, since the polished paper used is diamond based.

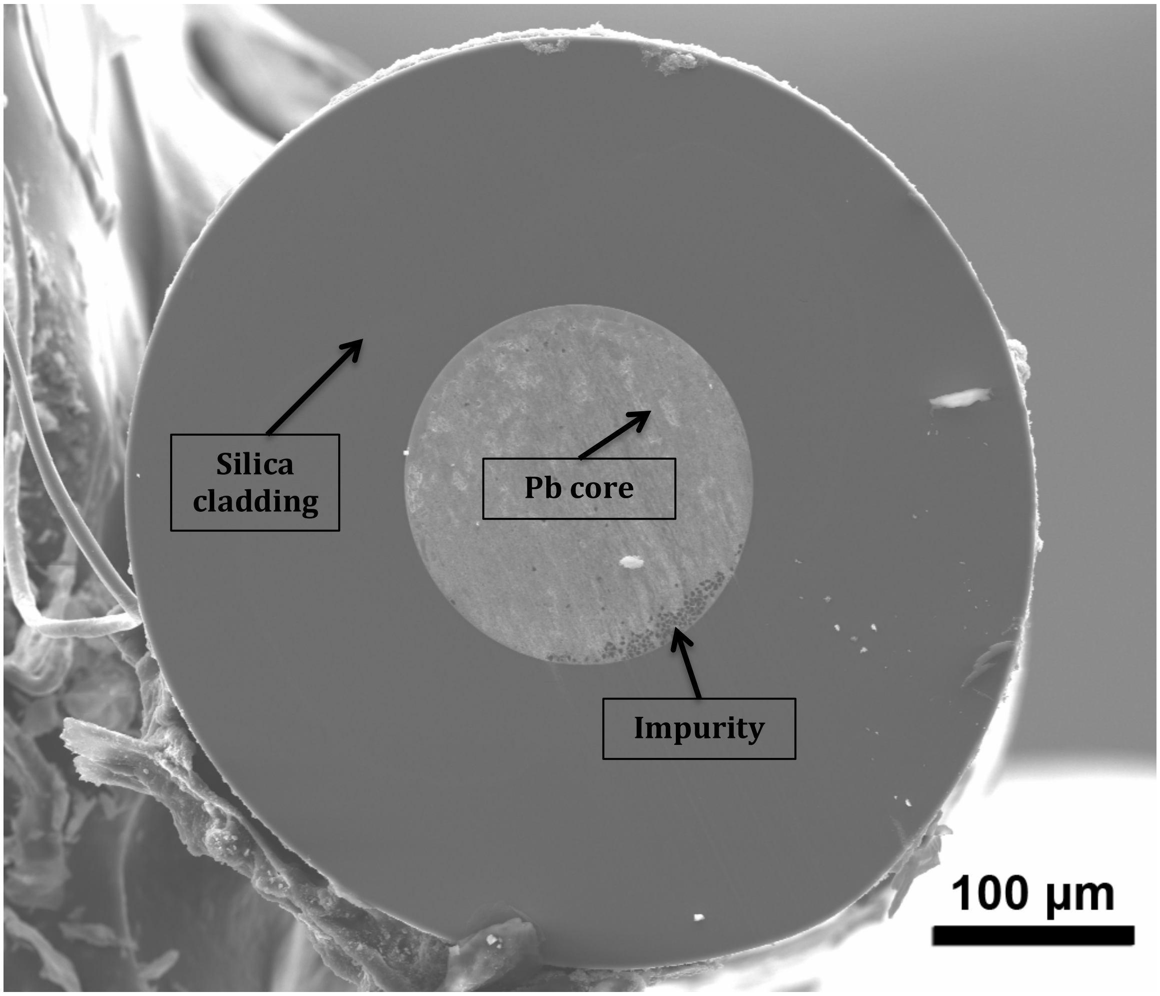

Figure 4.2 SEM image of cross section of the Pb core fiber with fused silica glass cladding.

The large magnification image of the Pb core is shown in Figure 4.3. In order to get the real condition of the Pb core, this image was taken without polishing to avoid the surface scratch since Pb is very soft. The image is of an unpolished fracture cross-section. There are no apparent pores in the core area and the core is relative dense.

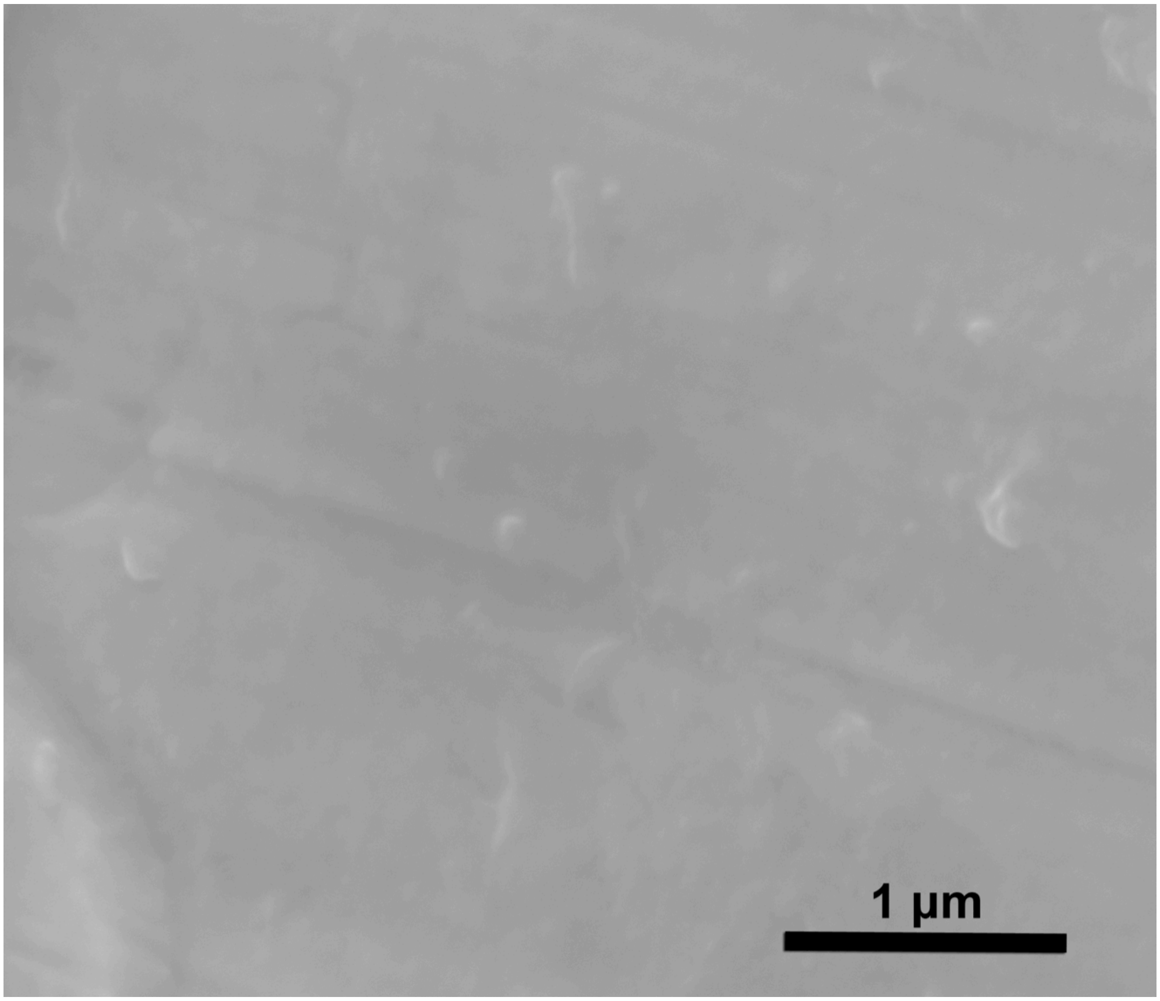

Figure 4.3 SEM image of large magnification (62355 X) for Pb core-taken without polishing.

### 4.3 Chemical composition

The EDS analysis of the Pb core fiber is shown in Figure 4.4. The point tested is located at the center of the core. As shown in the Figure, only Pb and oxygen elements were found in the core. In order to understand the oxygen in the Pb core, pure Pb was cut to the cross-section and immediately taken to EDS analysis so as to limit oxidation in air. The EDS analysis of the pure Pb is shown in Figure 4.5. As can be seen, the spectra of the Pb core and the pure Pb are very similar. That is the sign of limited oxygen in the Pb core region.

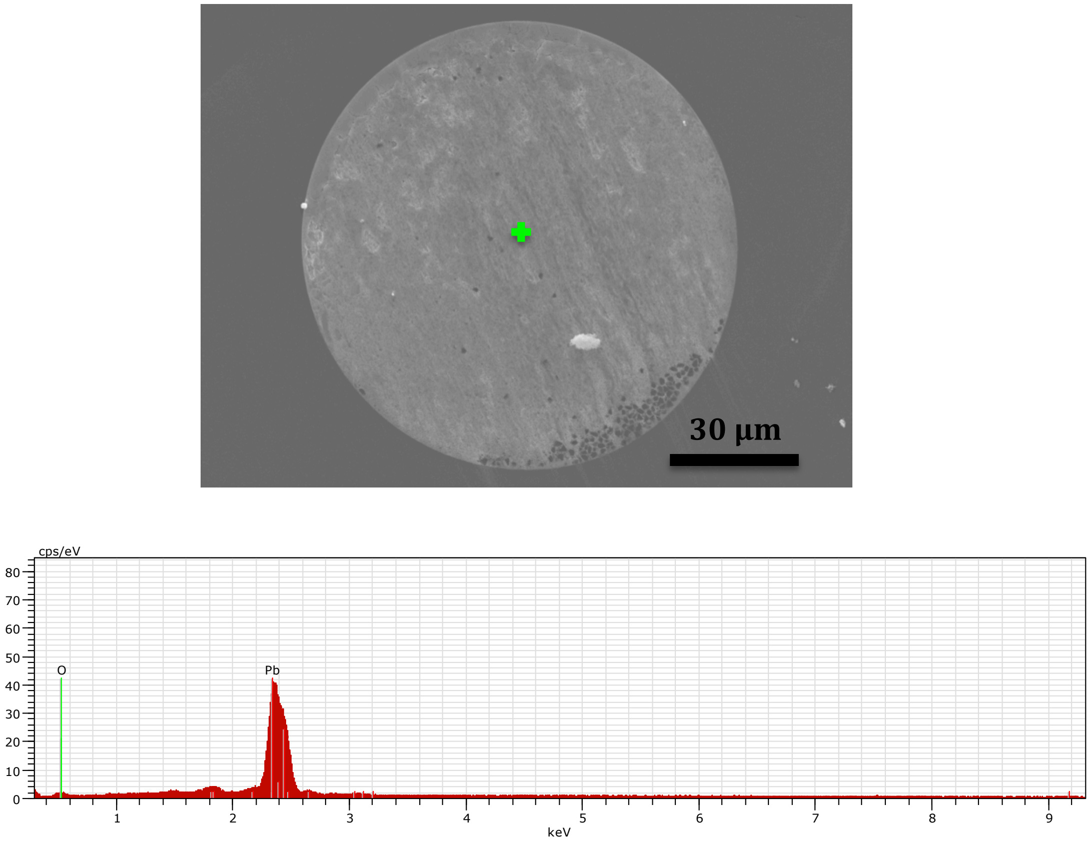

Figure 4.4 EDS analysis of the Pb core fiber: the image (top) shows the Pb core and the point with green color is the position where the measurement takes; the spectra (bottom) represent the elemental composition.

This kind of oxidation during synthesis could be avoided by applying a vacuum to the reaction system before processing. There are no silicon peaks seen in the spectra, indicating no silicon diffusion into the core region from the silica cladding.

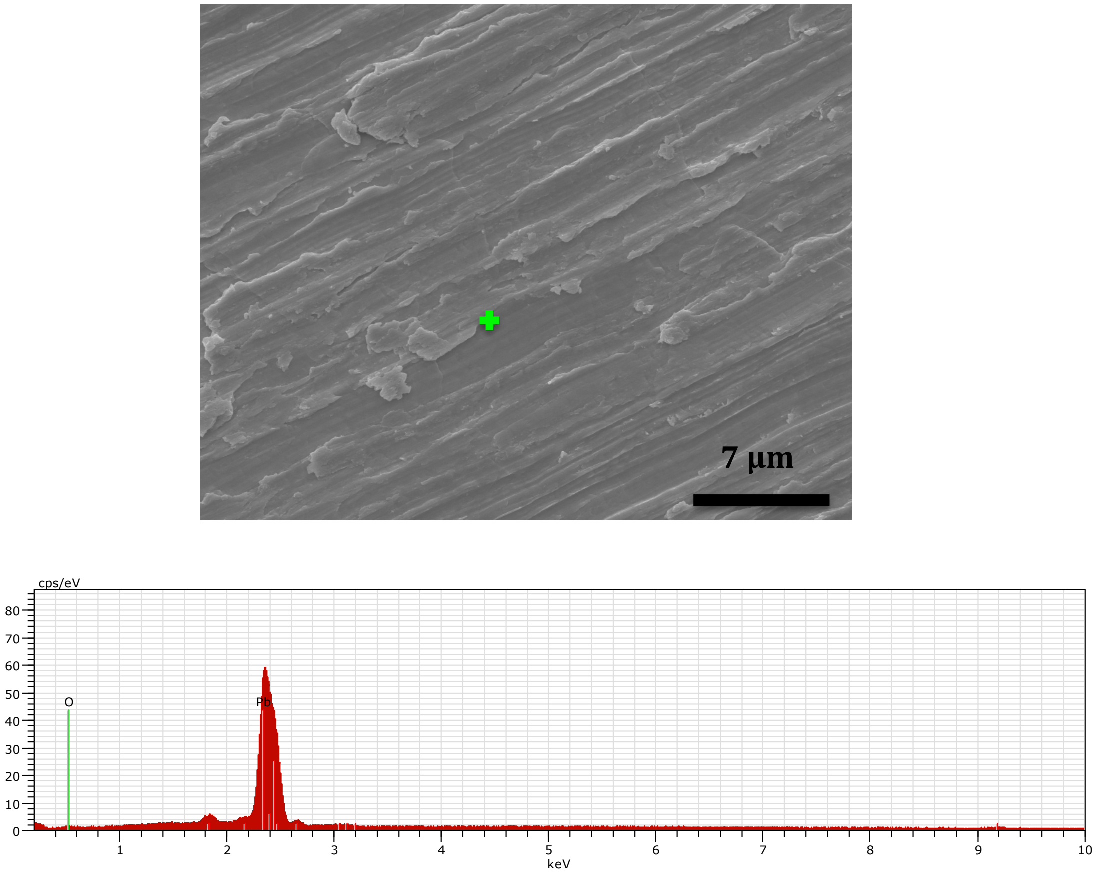

Figure 4.5 EDS analysis of the pure Pb material: the image (top) shows the pure Pb and the point with green color is the position where the measurement takes; the spectra (bottom) represent the elemental composition.

## 4.4 Interface effect

Figure 4.6 shows the EDS elemental mapping images between the Pb fiber core and fused silica cladding. The mapping images explain the diffusion behavior of elements across the interface of core and cladding. According to the images, Pb and Si show no apparent diffusion behavior across the interface line, which is also confirmed by EDS chemical composition spectra above.

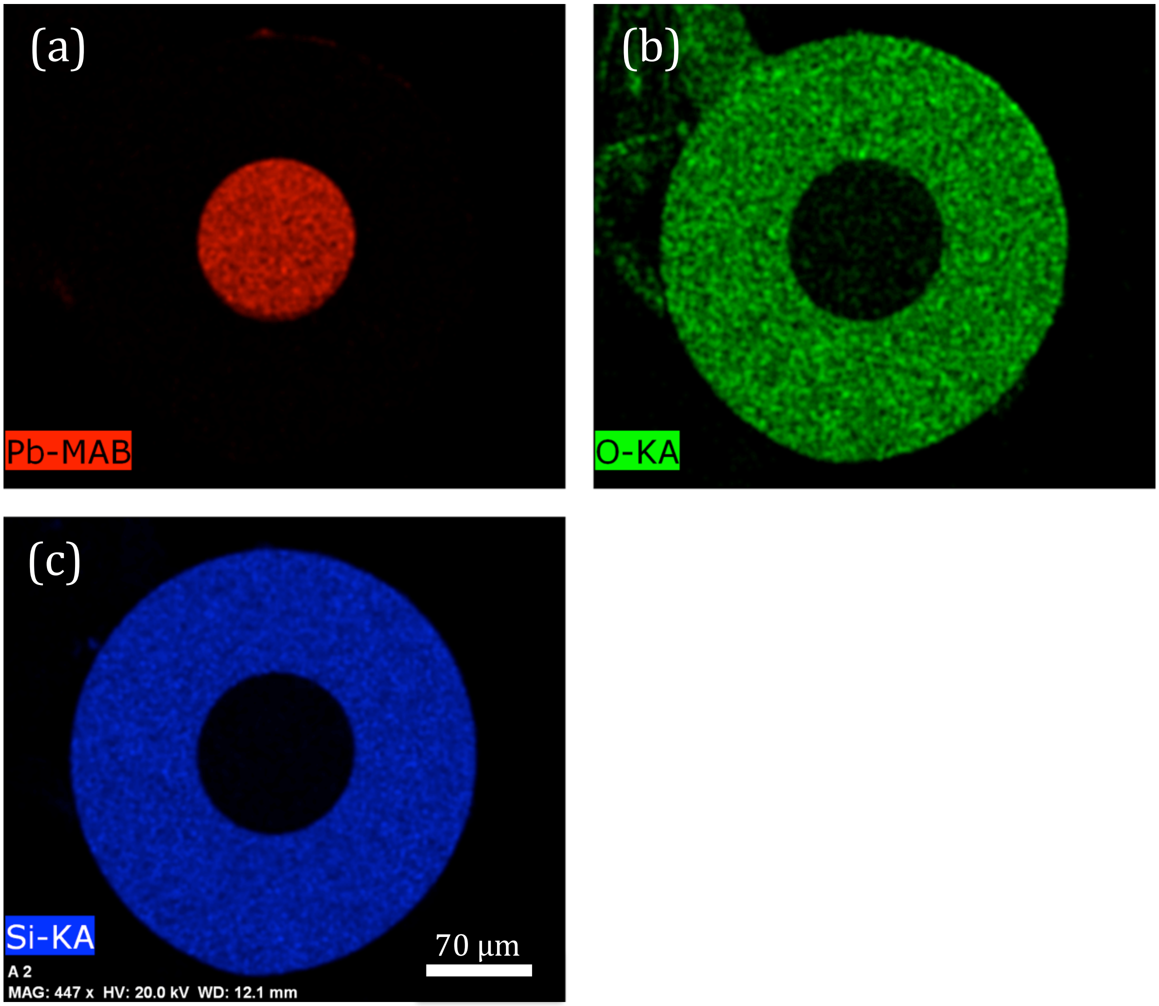

Figure 4.6 EDS elemental mapping between the Pb core and fused silica cladding, a) Pb-red, b) O-green, c) Si-blue.

Elemental analysis was performed on a cross section of the fiber in order to determine the extent to which the diffusion occurs during the draw process between the softened glass cladding and the molten Pb core. The EDS line scan of the Pb core fiber shown in Figure 4.7 is further used to investigate the diffusion behavior. The green line color across the fiber in the SEM image below represents the position where the measurement takes. The red, blue and green line colors in the spectra represent the Pb, Si and O, respectively. It can be concluded from the spectra that Pb is present in the core region and there is no apparent Pb in the cladding region. At the interface of the cladding and the Pb core, the Si amount suddenly drops to near zero and Pb increases from zero percent to a relatively stable amount (from left to right). The diffusion behavior is also highly affected by processing temperatures because of the relationship between the driving force for diffusion and temperature[71, 72].

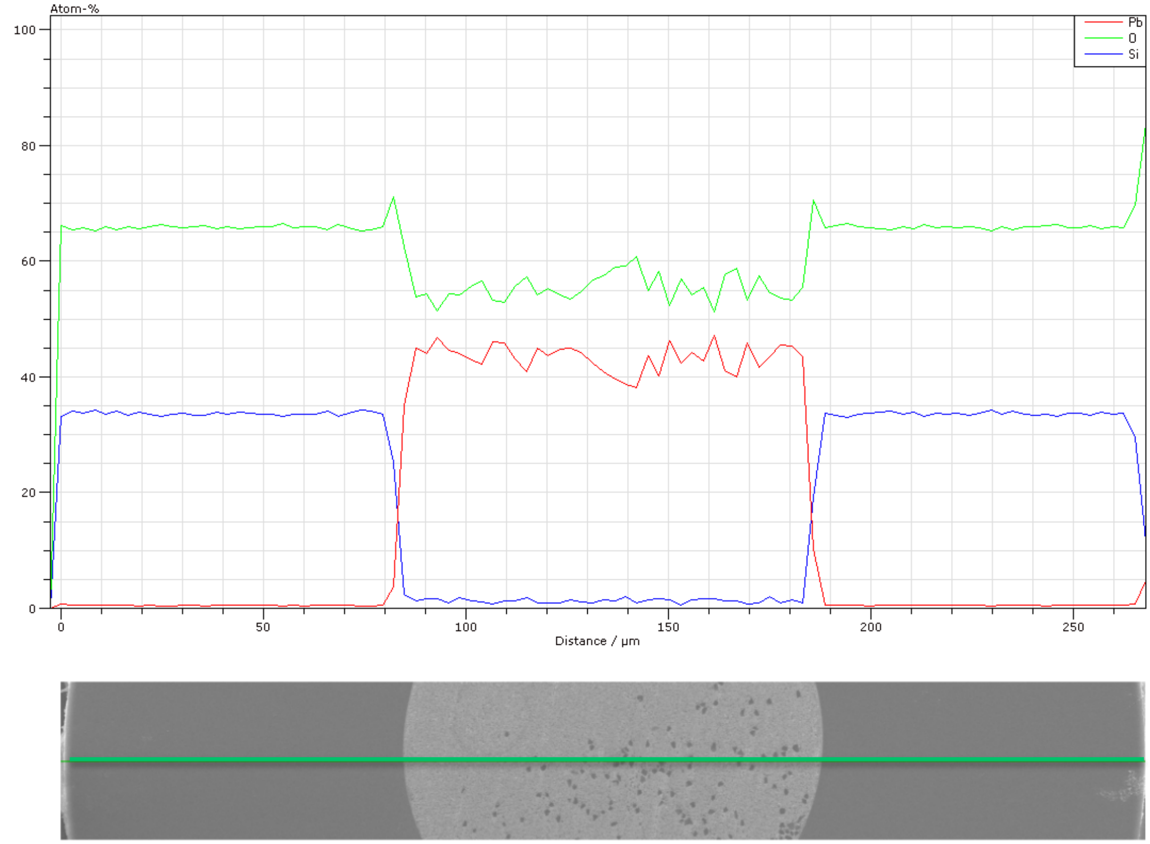

Figure 4.7 EDS line scan of the Pb core fiber, atomic percent versus distance on the cross section of the Pb core fiber: Pb-red, O-green, Si-blue. The green line in the lower image shows the position of measurement.

## 4.5 Superconductivity

In order to investigate the superconductivity of the Pb core fiber, a baseline measurement was performed with the commercially available Pb wire (diameter = 2 mm) in a liquid helium bath to compare with the prepared Pb core fiber.

Superconducting fibers with core diameters of approximately 800 microns were tested with and without the fused silica cladding.

The primary vertical axis is the resistance of the Pb core sample and the secondary vertical axis is the resistance of the commercial Pb wire. As seen in Figure 4.8, a graph in the temperature range of the superconducting transition can also be seen in the bottom right corner of the graph. All samples maintain a critical temperature of approximately 4-8 K. The resistance of the commercial Pb wire disappeared at temperatures on the order of 7.2 K. The superconducting Pb core fibers appeared to demonstrate a slightly lower Tc on the order of 4-6 K.

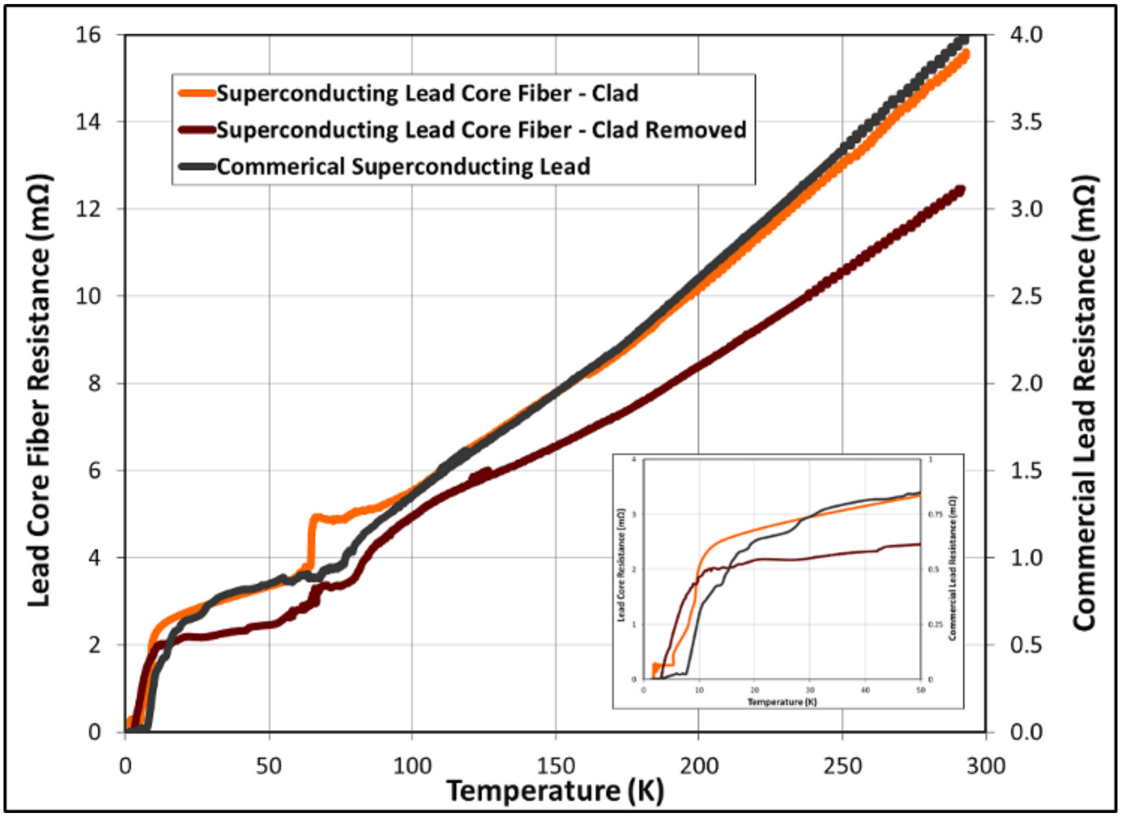

Figure 4.8 Electrical resistance as a function of temperature for (a) commercial Pb wire-grey, (b) Pb core fiber with the fused silica clad-orange, and (c) Pb core fiber with the fused silica clad removed prior to testing-brown.

The slight decrease in the critical temperature could be attributed to impurities and/or defects incorporated during fiber processing. Measurement errors were also possible due to thermal electromotive forces, external electromagnetic radiation, Faraday currents, and the degradation of the electrical contacts, as well as basic errors in the experimental set-up[73, 74].

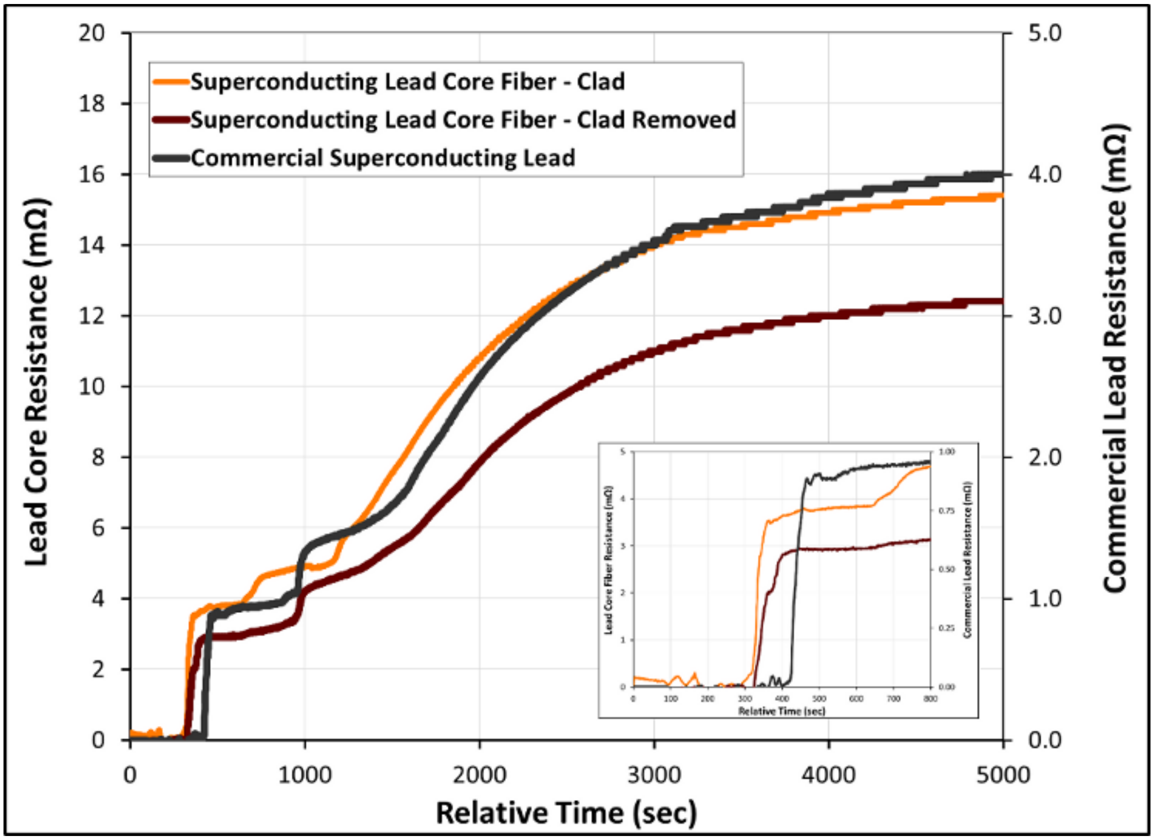

Figure 4.9 Electrical resistance measurements as a relative function of time for (a) commercial Pb wire baseline sample-grey, (b) Pb core superconducting fiber with the fused silica clad-orange, and (c) Pb core superconducting fiber with the fused silica clad removed prior to testing-brown.

In an effort to isolate any possible temperature measurement artifacts, the resistance of all the samples was also evaluated as a function of time upon natural warming to room temperature. As seen in Figure 4.9, the primary vertical axis is the resistance of the Pb core samples and the secondary vertical axis is the resistance of the commercial Pb wire. A graph in the range of the superconducting transition can also be seen in the bottom right corner of the graph. All samples demonstrate a similar transition to superconductivity and resistance-time profile upon warming to room temperature. The Pb core fiber and commercial Pb wire exhibit similar transitions to superconductivity and resistance-time profiles. The critical temperature has been verified and extensively studied in the literature and is generally accepted as approximately 7.2 K, which is in good agreement with the measurements in this study.

# 5 YBCO Superconducting Core Fiber

## 5.1 Fiber fabrication

YBCO starts to melt around 1010 °C, and once melted, the viscosity remains high which shows limited flowability. This causes more difficulty with the YBCO core fiber fabrication than with the Pb core fiber. The temperature and duration of the heating before drawing significantly affect the final product since there is the possibility of decomposing. Processing condition must be controlled carefully. Figure 5.1 shows the image of the YBCO core fiber length prepared with the glass lathe. The fiber length of around 15 cm (~6 inch) has been obtained. The core area exhibits black color that changes with the decomposed state.

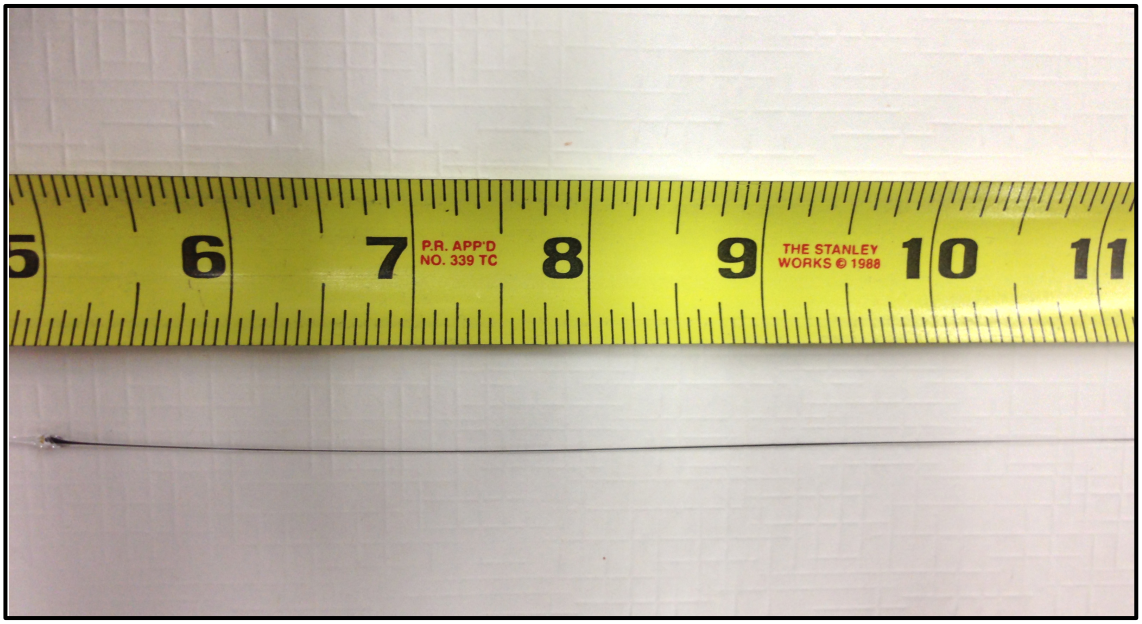

Figure 5.1 Photograph of the YBCO core fiber length, photo by author, 2014.

## 5.2 Surface morphology

The YBCO core fiber was successfully prepared via melt-draw technique on a glass lathe. An SEM image of the cross section of the YBCO core fiber with a fused silica glass cladding is shown in Figure 5.2. As can be seen, the fiber possesses good circularity and a clean interface between the YBCO core and the fused silica glass cladding. The fused silica cladding maintained a diameter of approximately 800 μm and a YBCO core diameter of 250 μm, respectively.

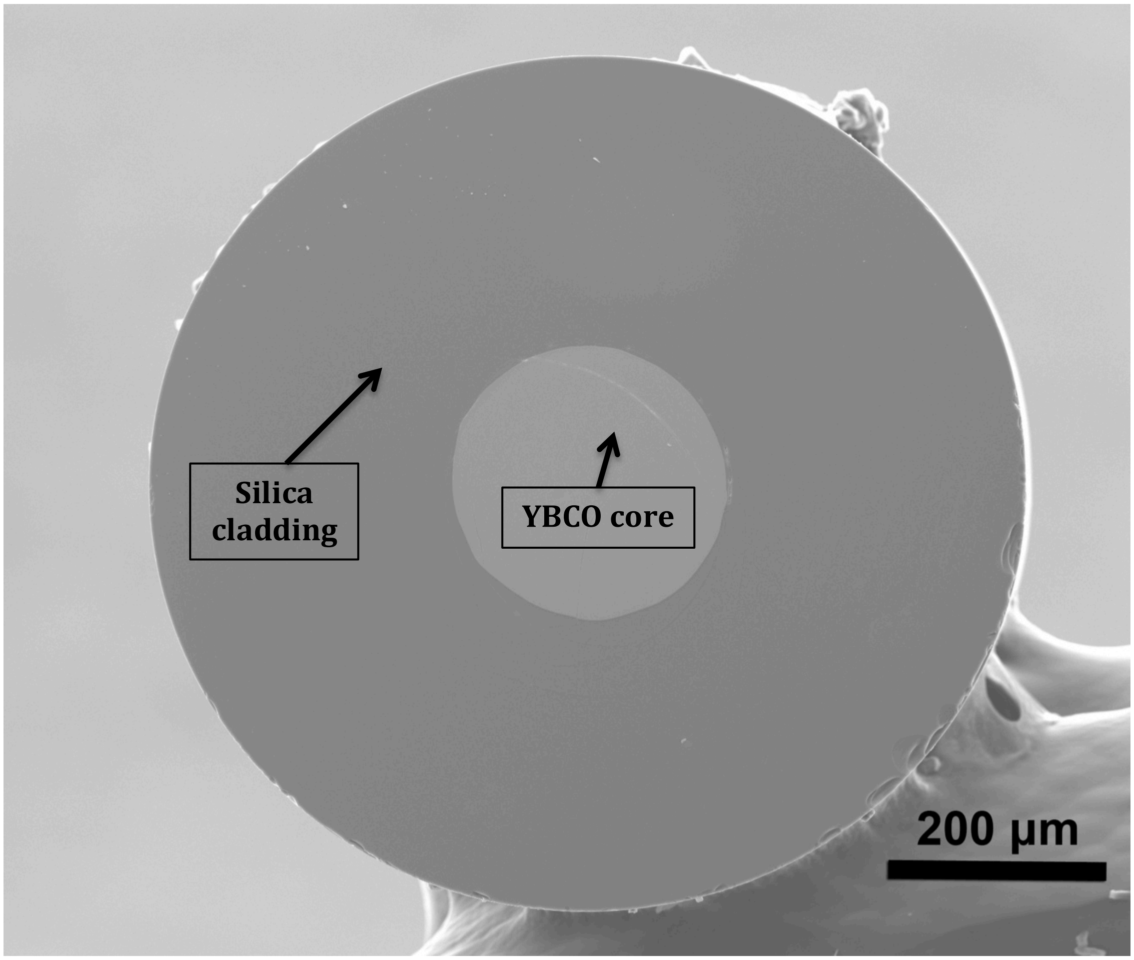

Figure 5.2 SEM image of cross section of the YBCO core fiber with fused silica glass cladding.

The high magnification image of the YBCO core is shown in Figure 5.3. The sample was prepared without polishing. The drawing temperature required for fused silica is above 2000 °C, which is much higher than the melting point of the YBCO (~1010 °C)[75]. The rapid solidification of the melt YBCO core upon fiberization shows no apparent pores and the core is relatively dense. However, decomposition may occur for YBCO in such high temperature [10]:

$$\mathrm{YBa_2Cu_3O_{6+x}} \rightarrow \frac{1}{2}\mathrm{Y_2O_3} + \mathrm{BaO} + \mathrm{CuO} \qquad (5)$$

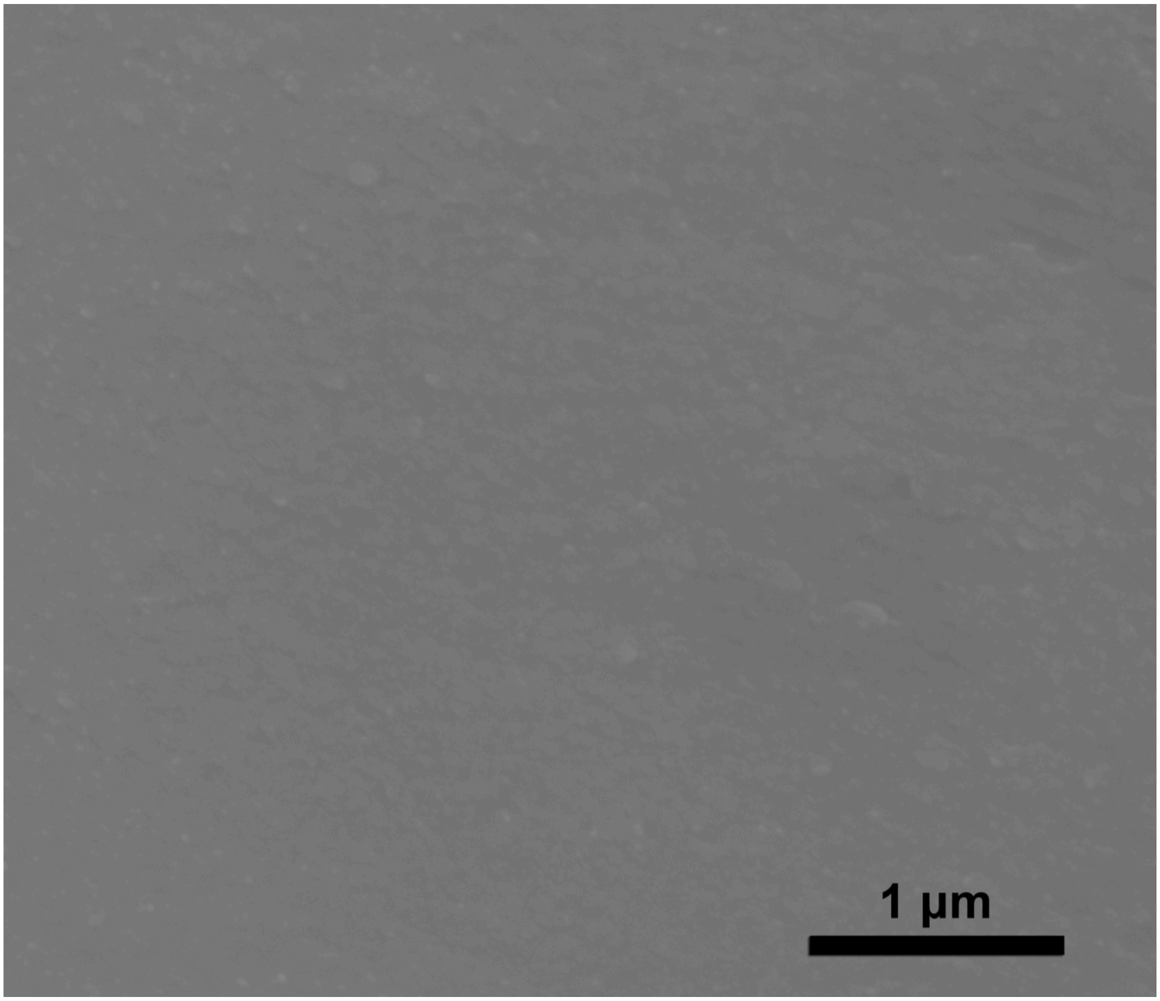

Figure 5.3 SEM image of high magnification (54605 X) for YBCO core-taken without polishing.

There may be changes in oxidation state of the YBCO phase, which is not superconductive, resulting from the reduction in oxygen content in the YBCO phase. So heat treatment is needed after the melting process to convert the non-superconducting phases back to the superconducting state.

## 5.3 Chemical composition

Figure 5.4 shows the EDS analysis of the YBCO core and Figure 5.5 shows the EDS analysis of the YBCO powder. According to these two spectra, they have similar peaks for Y, Ba, Cu and O. However, the Si peak in the spectra of the YBCO core is very obvious.

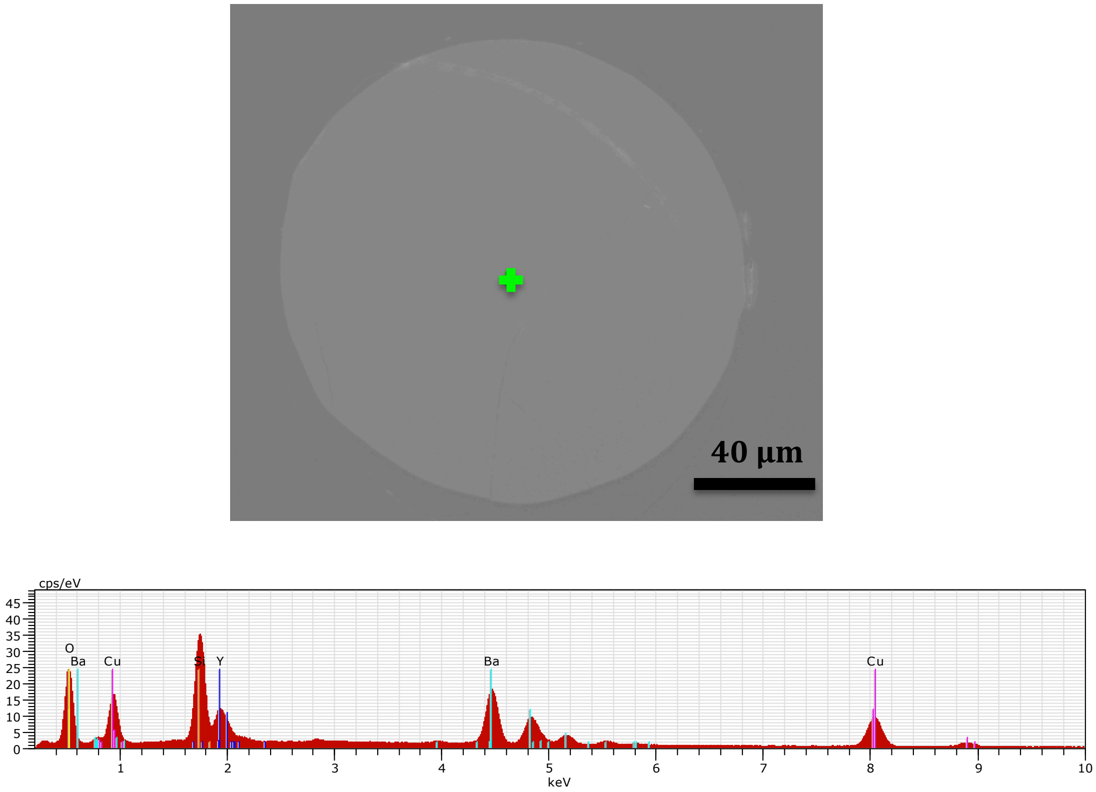

Figure 5.4 EDS analysis of the YBCO core fiber: the image (top) shows the YBCO core and the point with green color is the position of measurement; the spectra (bottom) represent the elemental composition.

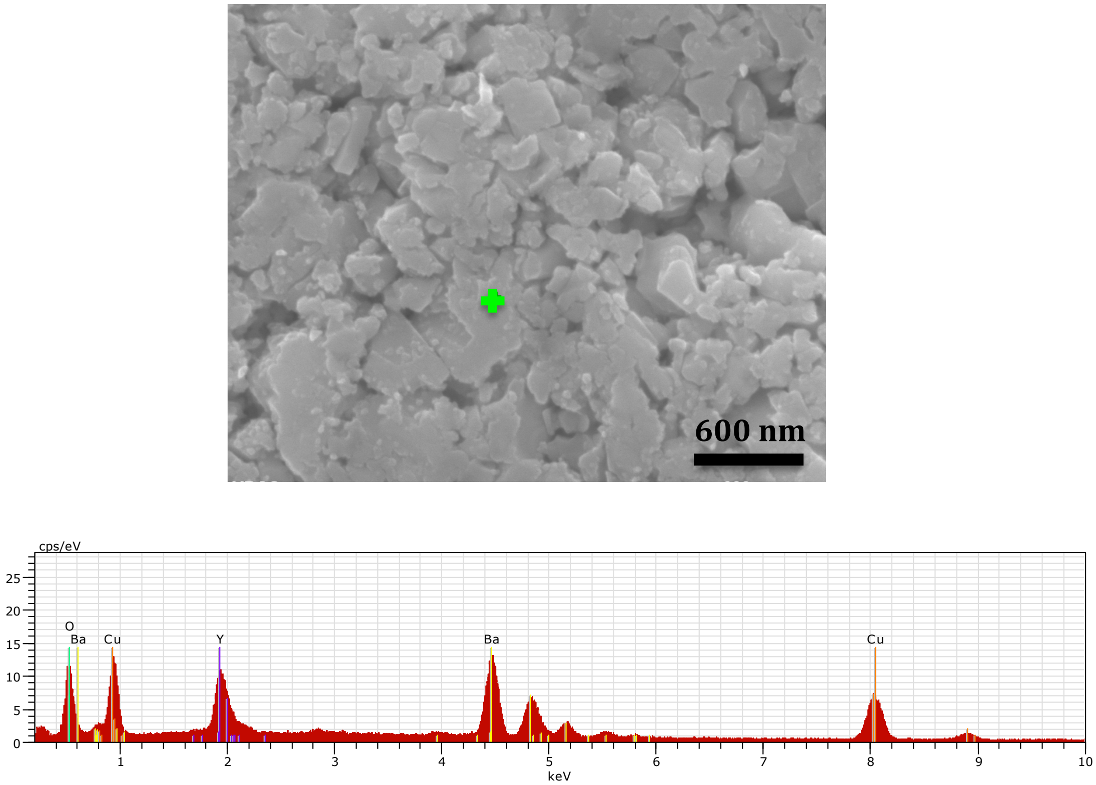

Figure 5.5 EDS analysis of the YBCO powder: the image (top) shows the YBCO powder and the point with green color is the position of measurement; the spectra (bottom) represent the elemental composition.

The quantitative composition of the YBCO core fiber is shown in Table 5-1. It is taken by averaging five measurements. The Y, Ba, Cu, O and Si have atomic percent about 4.79±0.26, 9.40±0.28, 12.30±0.58, 56.05±0.26, and 17.46±0.65, respectively. Y:Ba:Cu is not exactly proportional to 1:2:3 but very close (1:1.96:2.57), that could be affected by the interference of the close peak positions. The Si element detected in the spectra needs to be further investigated.

Table 5-1 Quantitative composition of the YBCO core by EDS.

| Element | Atomic % |
|---|---|
| Y | 4.79±0.26 |
| Ba | 9.40±0.28 |
| Cu | 12.30±0.58 |
| O | 56.05±0.26 |
| Si | 17.46±0.65 |

## 5.4 Interface effect

Figure 5.6 shows the EDS elemental mapping images between YBCO fiber core and fused silica cladding. The mapping images explain the interface effect of elements across the core and cladding. According to the images, Y, Ba, Cu are all present to some extent in the silica cladding. Also, significant Si is present in the core.

Elemental analysis was performed on a cross section of the fiber in order to determine the extent to which the interface interaction occurs during the melt-draw process between the softened glass cladding and the molten YBCO core. The EDS line-scan of the YBCO core is shown in Figure 5.7. The green line color across the fiber in the image below represents the position where the measurement was taken, along the line from the left edge to right edge of cladding. The red, green, blue, bluish green and purple line colors in the spectra represent the Y, Ba, Cu, O and Si, respectively. It is noted that Y, Ba, Cu elements present in the cladding region during high temperature processing based on the EDS line scan. It is also seen that Si is present in the core region, but decreases to a lower amount than in the cladding. Most of these results match the EDS mapping.

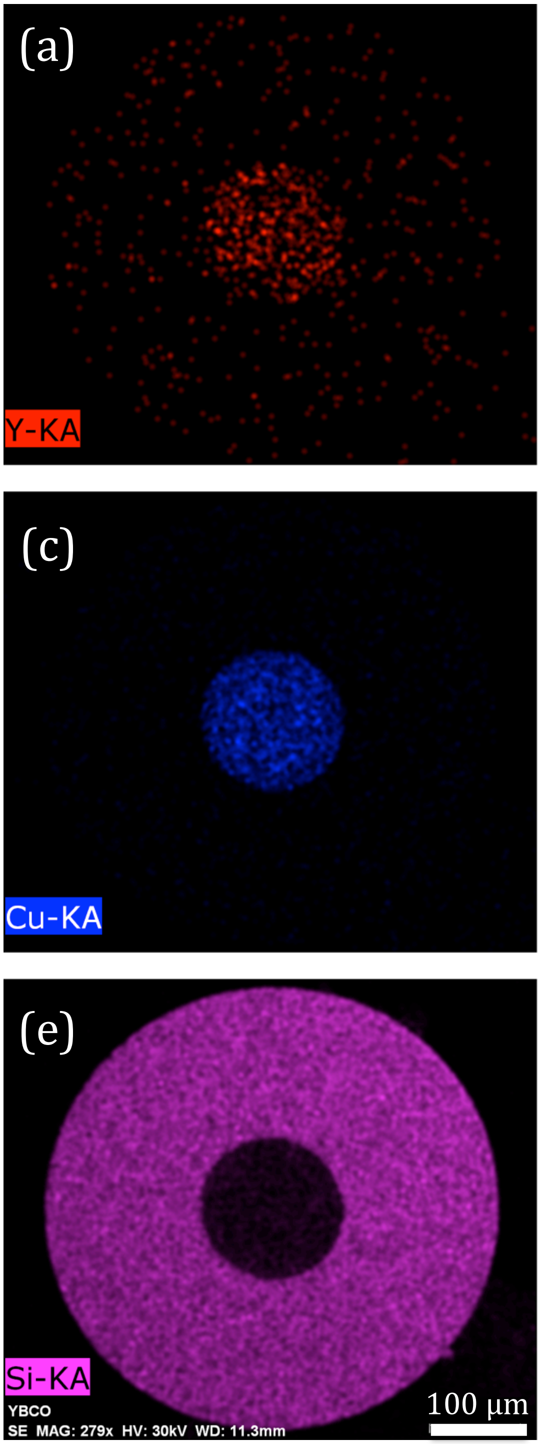

Figure 5.6 EDS elemental mapping between YBCO core and fused silica cladding, a) Y-red, b) Ba-green, c) Cu-blue, d) O- bluish green and e) Si-purple.

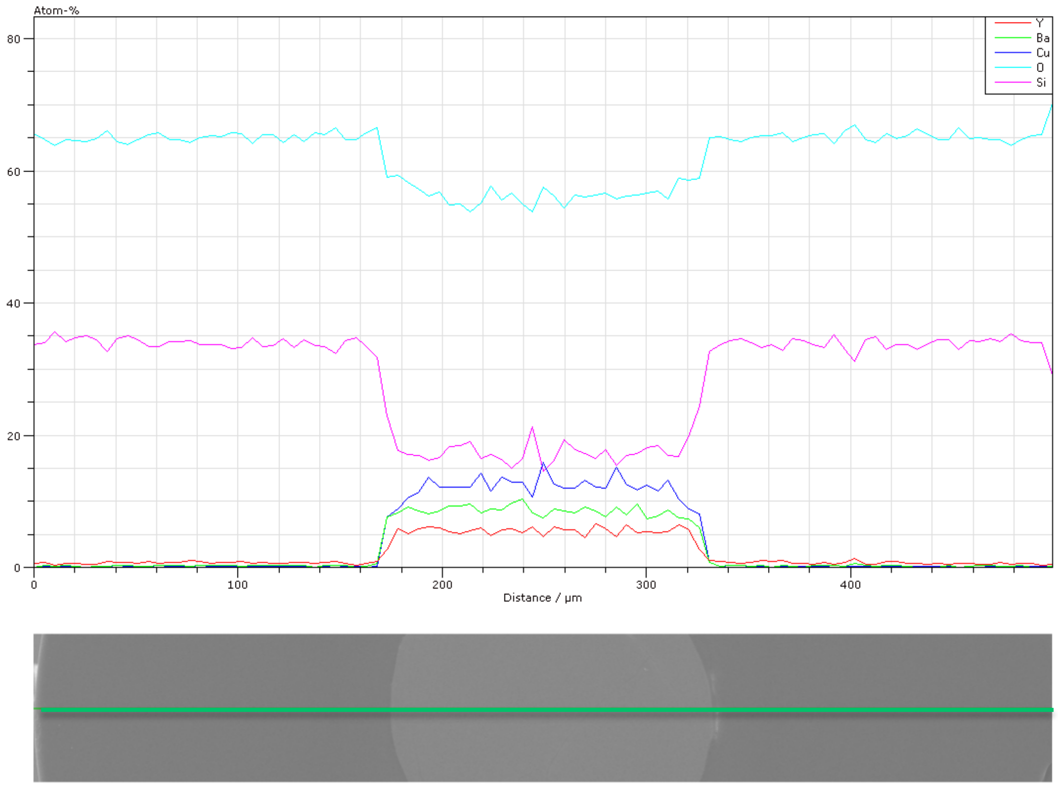

Figure 5.7 EDS line scan of the YBCO core, atomic percent versus distance of the cross section of the YBCO core fiber: Y-red, Ba-green, Cu-blue, O-bluish green and Si-purple.

However, the mapping image of the Figure 5.6 doesn't show high levels of Si in the core region but around 17 atomic % is present in the line scan. It is believed there is a large amount of Si inside the core region since the EDS mapping image is just a rough detection for the elements distributions and is affected by the contrast of the image. It has been reported that the $SiO_2$ does not react with the YBCO and also does not enter the structure of the YBCO during high temperature treatment[76]. During the melting process of around 2000 °C, the YBCO core melts and the fused silica cladding also tends to melt. The possible hypothesis for Si exists in the YBCO core is that the fused silica mixes into the YBCO core after melting but the phases separate after fast cooling. Before reaching a conclusion, however, further characterization is still needed.

## 5.5 Superconductivity

YBCO represents the most important high temperature superconductor because of it was the first superconductor exhibiting a transition point higher than the evaporation temperature of liquid nitrogen. During the melt-draw process, the YBCO core decomposes rapidly and thus loses superconductivity. The fiber core without additional heat treatment was confirmed to be not superconductive experimentally. So the optimum heat treatment procedure needed to be determined to recover the superconductive property.

As seen in Figure 5.8, the resistance of the YBCO versus temperature was used to compare the superconductivity state (both YBCO superconducting core fiber and commercial YBCO bulk). For YBCO materials, the resistance is larger than the Pb core fiber in the non-superconducting region. The YBCO commercial bulk and YBCO core fiber exhibit a similar transition curve. The YBCO core fiber resistance is higher than YBCO bulk because of the size. There is a sharp decline of the resistance at around 90 K, which is the evidence of its superconductivity. The successful confirmation of the superconductivity of the YBCO core with the glass cladding is a very important result as it is first time that anyone has demonstrated this in an optical fiber.

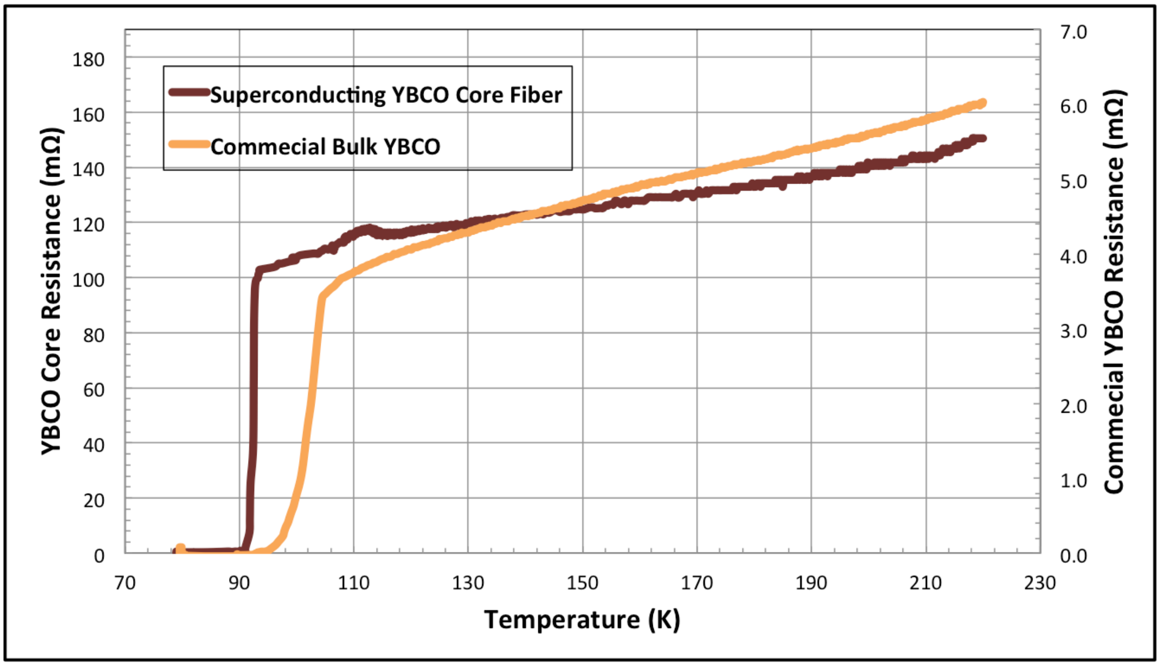

Figure 5.8 Electrical resistance as a function of temperature for commercial YBCO bulk disk and a superconducting YBCO core fiber with fused silica clad. The primary vertical axis is the resistance of the YBCO core sample and the secondary vertical axis is the resistance of the commercial high temperature-superconducting sample. All samples maintained a Tc of approximately 90-100 K.

# 6 Hollow Fiber for Efficient Cooling

## 6.1 Microstructure of the Pb core holey fiber

An optical micrograph of the ordered hole superconducting Pb fiber is shown in Figure 6.1. The 900-micron fiber maintains a fused silica cladding containing eleven ordered holes and several voids surrounding a Pb core with a diameter of approximately 230 microns. Some of the holes are filled with Pb particles because of the polishing step. The darker area is the holes that help with transferring liquid helium. In an effort to assure liquid helium transport, the fiber was fabricated with a significant percentage of additional void space.

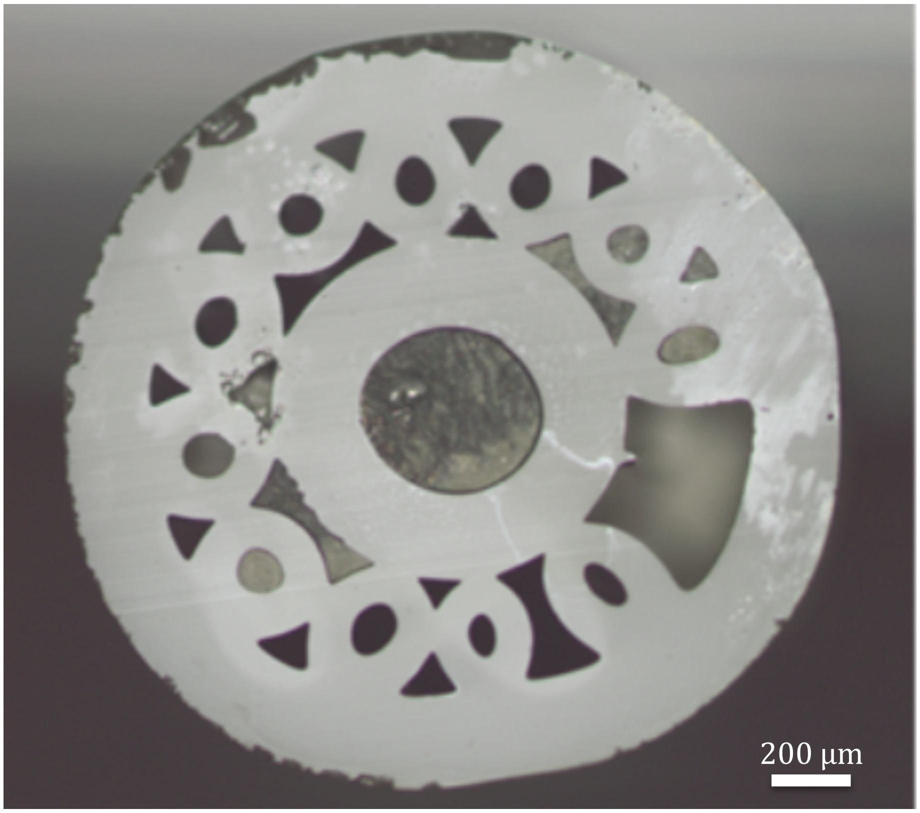

Figure 6.1 Optical micrograph of ordered hole superconducting fiber.

## 6.2 Superconductivity of the Pb core holey fiber

Superconductivity was demonstrated in the holey Pb core fiber via the aforementioned modified test set-up upon liquid helium infiltration, as seen in Figure 6.2. The temperature of the surface of the Pb core at both ends of the fiber sample at the superconducting transition was approximately 30-40 K, which is higher than the critical temperature of the Pb, Tc = 7.2K. The significant temperature different of 23-33 K is attributed to the positioning of the thermocouple. It was not bonded to the Pb material, and measured the temperature of the "environment" near the Pb core, as opposed to on the Pb core. So it is the artifact of the position of the measurement.

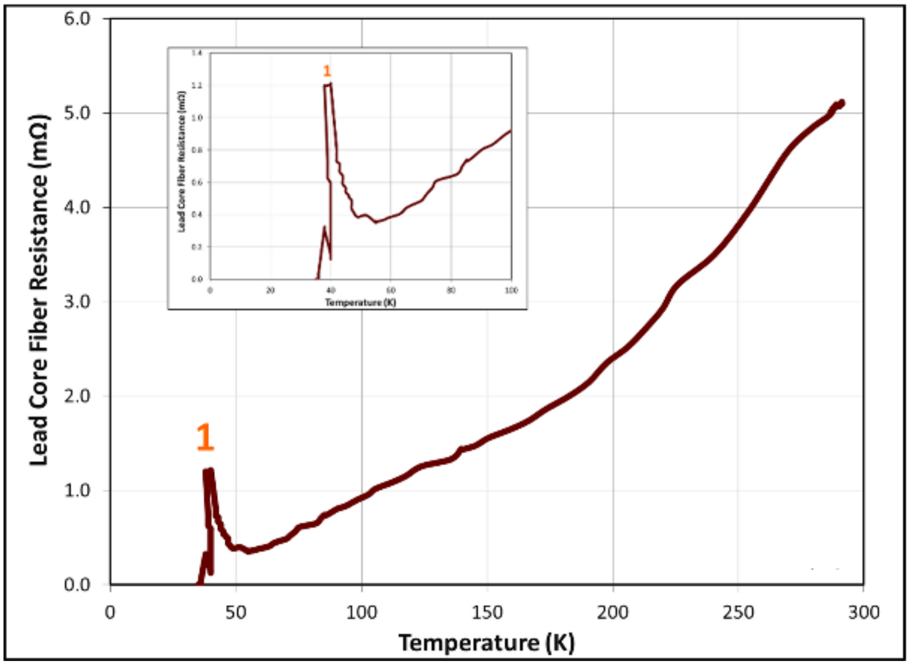

Figure 6.2 Resistance as a function of temperature upon liquid helium injection into the cladding holes of a Pb superconducting fiber. The superconducting transition occurs at temperature of 35K on the outer fiber diameter.

Although, the liquid helium readily permeated the holes of the fiber[77-79] the testing demonstrated that a minimum liquid helium flow rate and/or pressure and completely sealed system is required to assure adequate cooling of the fiber with a specified geometry. Zero resistance was maintained for several seconds once the liquid helium flow was turned off and then naturally warmed to room temperature. The necessary cryogenic cooling for superconductivity was readily achieved via liquid helium infiltration of the porous cladding with properly sealed delivery system.

## 6.3 1-D single-phase steady state heat transfer model

The relation of the mass flow rate to the length of the tube that keeps the cryogenic liquid was further investigated. A dimensional (1-D) single-phase steady state heat transfer model was adopted to estimate the theoretical liquid nitrogen transfer inside glass tube. The model was developed under the following assumptions:

- The capillary tube is horizontal (gravity effects are neglected), and of constant cross section.
- The flow in the capillary tube is steady, one-dimensional, and adiabatic with no externally applied work.
- No axial conduction.
- The fluids inside the tube are incompressible, consistent and no phase chage (assume no change on properties).

Figure 6.3 shows the model of the capillary tube. Liquid nitrogen goes into the tube from the inlet with temperature $T_{in}$ and goes out with temperature $T_{out}$. Heat transfer mechanism was separated into three parts: natural convection between air and the outer surface of the tube wall, heat conduction through the tube wall and forced convection between liquid nitrogen and the inner surface of the tube wall. They are investigated separately as below. The steady state is defined by:

$$\frac{dT}{dt} = 0$$

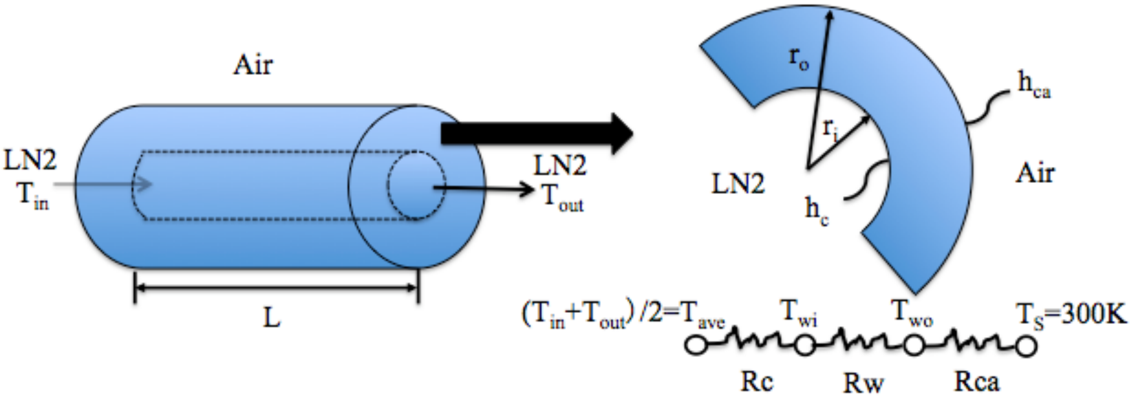

Figure 6.3 The schematic of the capillary tube for cryogenic liquid transfer.

### 6.3.1 Natural air convection at outer surface of the tube

The air convection outside the tube can be treated as free convection over the horizontal cylinders. The Grashof number is used to correlate free convection instead of the Reynolds number. For free convection over the horizontal tube[80]:

$$\mathrm{Gr} = \frac{g\beta_t\rho^2(T_s - T_{wo}){D_o}^3}{\mu^2} \tag{6}$$

The g is the local acceleration due to gravity; $\beta_t$ is the volumetric thermal expansion coefficient for the air; ρ is the density of the air; $T_s$ is the environmental temperature; $T_{wo}$ is the outer surface temperature of the tube wall; $D_o$ is the outer diameter of the tube; μ is the viscosity of the air. For gases, the thermal expansion coefficient may be approximated by

$$\beta_t = 1/T_m \tag{7}$$

where $T_m$ is the mean film absolute temperature. The correlations are in terms of the Rayleigh number, Ra = GrPr (Pr is Prandtl number $\mathrm{Pr} = \frac{C_p\mu}{k}$).

For the laminar regime ($10^{-4} < \mathrm{GrPr} < 10^9$), the heat transfer correlation is as follows[81]:

$$\mathrm{Nu_{air}} = 0.36 + \frac{0.518(\mathrm{GrPr})^{1/4}}{[1 + (0.559/\mathrm{Pr})^{9/16}]^{4/9}} \tag{8}$$

where $\mathrm{Nu_{air}}$ is Nusselt number. The convective coefficient is:

$$\mathrm{h_{ca}} = \frac{\mathrm{Nu_{air}k_a}}{\mathrm{D_o}} \tag{9}$$

where $\mathrm{h_{ca}}$ is air convective heat transfer coefficient; $\mathrm{k_a}$ is the thermal conductivity estimated by the temperature $\mathrm{T_m}$.

The surface area of the tube is:

$$\mathrm{A_{wo}} = \pi \mathrm{D_o L} \tag{10}$$

where $\mathrm{A_{wo}}$ is the outer surface area of the tube; L is the length of the tube. So the heat transfer rate is found from the convection rate equation as follows:

$$\mathrm{Q_{ca}} = \mathrm{h_{ca}A_{wo}(T_s - T_{wo})} \tag{11}$$

where $\mathrm{Q_{ca}}$ is the convective air heat transfer rate.

### 6.3.2 Conduction through the tube wall

The conduction heat transfer through the tube wall can be derived according to Fourier rate equation:

$$\mathrm{Q_d} = -\mathrm{k_t A(x)} \frac{\mathrm{dT}}{\mathrm{dx}} \tag{12}$$

where $\mathrm{k_t}$ is the thermal conductivity of tube materials evaluated at mean temperature of the tube wall; A is conduction area.

For steady-state, the heat transfer rate is constant, so we may integrate to obtain

$$\mathrm{Q_d} \int_{x1}^{x2} (\mathrm{dx/A}) = \int_{\mathrm{T_{wi}}}^{\mathrm{T_{wo}}} \mathrm{k_t\, dT} \tag{13}$$

where x1 is the coordinate at the outer surface of the tube with $T_{wo}$; x2 is the coordinate at the inner surface of the tube with $T_{wi}$.

The conduction shape factor S is defined by

$$\frac{1}{S} = \int_{x1}^{x2} (dx/A) \qquad (14)$$

As the conduction area for the uniform tube is $A(r)=2\pi rL$, the equation becomes:

$$S = \frac{2\pi L}{\ln(D_0/D_i)} \qquad (15)$$

where L is the length of the tube, $D_0$ is the outer diameter, and $D_i$ is the inner diameter.

The integral on the right side of equation ( 13 ) may be written as follows in terms of two integrals:

$$\int_{T_{wi}}^{T_{wo}} k_t \, dT = \int_{0}^{T_{wo}} k_t \, dT - \int_{0}^{T_{wi}} k_t \, dT \qquad (16)$$

So, the expression for one-dimensional conduction heat transfer, equation ( 13 ) may be written in the final form as

$$Q_d = S(K_{wo} - K_{wi}) = Sk_m(T_{wo} - T_{wi}) \qquad (17)$$

where $Q_d$ is the conductive heat transfer rate through the tube wall; $K_{wo}$ and $K_{wi}$ are the thermal conductivity integrals evaluated at the temperatures $T_{wo}$ and $T_{wi}$, respectively; $k_m$ is the mean thermal conductivity of the tube wall.

### 6.3.3 Cryogenic fluid forced convection at inner surface of the tube

The cryogenic fluids flow inside the tube can be treated as forced convection heat transfer. So, it is the first priority to determine if it is laminar or turbulent flow.

The mass flow rate per unit cross-sectional area is the following:

$$\mathrm{G} = \frac{\mathrm{m}}{\mathrm{A_c}} \tag{18}$$

where m is the mass flow rate per unit time; $A_c$ is the convective surface area. The Reynolds number is

$$Re = \frac{D_i G}{\mu_L} \tag{19}$$

where $D_i$ is the inner diameter of the tube; $\mu_L$ is the viscosity of the fluid. According to the Reynolds number, the flow can be divided into Laminar flow (Re<2300), turbulent flow (Re>3000) and transition region. For laminar flows the thermal entrance length is a function of the Reynolds number and the Prandtle number, $\frac{x}{D_i} = 0.05RePr$, where x is the thermal entry length. While, the entrance length for turbulent flow is independent of the Prandtl number with $\frac{x}{D_i} = 10$.

When the flow is laminar ($Re < 2300$) in a short tube (L/D<60) within thermal entry length, and the properties were evaluated at the appropriate temperature. The friction factor and heat transfer coefficient correlations are as follows[82]:

$$Nu = 3.657 + \frac{0.0668Gz}{1 + 0.04Gz^{2/3}} \tag{21}$$

$$f = \frac{64}{Re} \tag{20}$$

When the flow region combines the entry length, the following equation will be used if $Gz^{1/3}(\frac{\mu}{\mu_w})^{0.14} > 2$, otherwise $Nu = 3.66$:[83]

$$Nu = 1.86 * Gz^{1/3}(\frac{\mu}{\mu_w})^{0.14} \tag{22}$$

where $\mu$ is the viscosity of liquid nitrogen evaluated at the average or bulk temperature, and $\mu_w$ is the viscosity of inner wall evaluated at the wall temperature.

All of the fluid properties are evaluated at the average or bulk temperature, $T_{ave} = \frac{T_{in}+T_{out}}{2}$. The quantity Gz is the Graetz number,

$$Gz = RePr(\frac{D_i}{L}) \tag{23}$$

where $T_{in}$ is the temperature of liquid nitrogen inlet; $T_{out}$ is the temperature of liquid nitrogen outlet; L is the length of the tube. And the Nusselt number is $Nu = \frac{h_c * D_i}{k_L}$.

So the convective heat transfer coefficient is found as follows for laminar flow as Hausen correlation[84] when in thermal entry length for short tube:

$$h_c = (3.657 + \frac{0.0668Gz}{1 + 0.04Gz^{2/3}})\frac{k_L}{D_i} \tag{24}$$

where $h_c$ is cryogenic fluid convective heat transfer coefficient; $k_L$ is the thermal conductivity estimated by the average temperature of cryogenic fluid inside the tube $T_{ave}$.

When the flow is turbulent ($\mathrm{Re} > 3000$), the entry length is only 10 times of flow diameter in tube; we can neglect the entrance effect. And Gnielinski [85] gives a correction for Nusselt number used for $3000 \leq \mathrm{Re} \leq 5 * 10^6$ in a smooth tube:

$$f = \frac{1}{(1.82 * Log_{10}Re - 1.64)^2}$$

$$Nu = \frac{\left(\frac{\mathrm{f}}{8}\right) * (\mathrm{Re} - 1000) * \mathrm{Pr}}{1 + 12.7 * \sqrt{\frac{f}{8}} * (Pr^{\frac{2}{3}} - 1)} \tag{25}$$

So for a turbulent flow, the heat transfer coefficient is:

$$h_c = \frac{\left(\frac{\mathrm{f}}{8}\right) * (\mathrm{Re} - 1000) * \mathrm{Pr}}{1 + 12.7 * \sqrt{\frac{f}{8}} * (Pr^{\frac{2}{3}} - 1)}\frac{k_L}{D_i} \tag{26}$$

The surface area of the inner wall of the tube is:

$$A_{wi} = \pi D_i L \tag{27}$$

The convective heat transfer rate is:

$$Q_c = h_c A_{wi}(T_{wi} - T_{ave}) \tag{28}$$

where $Q_c$ is the convective fluid heat transfer rate; $T_{wi}$ is inner wall temperature.

### 6.3.4 Overall heat transfer

As discussed above, the following equations have been found:

$$Q_{ca} = h_{ca} A_{wo}(T_s - T_{wo})$$

$$Q_d = S(K_{wo} - K_{wi}) = S k_m (T_{wo} - T_{wi})$$

$$Q_c = h_c A_{wi}(T_{wi} - T_{ave})$$

For these three heat transfer mechanisms, the heat transfer is in series. At steady-state condition, the heat transfer rate through each part is equated. The overall heat transfer rate is:

$$Q_{in} = Q_{ca} = Q_d = Q_c \tag{29}$$

where $Q_{in}$ is the overall heat transfer rate from the environment to the tube at steady state. The following equations are obtained:

$$T_s - T_{wo} = \frac{Q_{in}}{h_{ca} A_{wo}}$$

$$T_{wo} - T_{wi} = \frac{Q_{in}}{S k_m}$$

$$T_{wi} - T_{ave} = \frac{Q_{in}}{h_c A_{wi}}$$

And $\Delta T = (T_{wi} - T_{ave}) + (T_{wo} - T_{wi}) + (T_s - T_{wo}) = T_s - T_{ave}$

So the overall heat transfer rate can be concluded by:

$$Q_{in} = \frac{T_s - T_{ave}}{\frac{1}{Sk_{\mathrm{m}}} + \frac{1}{h_c A_{wi}} + \frac{1}{h_c A_{wo}}} \tag{30}$$

The heat transfer rate acts on cryogenic fluid inside the tube may be applied as follows in steady state:

$$Q_{out} = mC_p(T_{out} - T_{in}) \tag{31}$$

where $Q_{out}$ is the energy taken out by heat liquid nitrogen. According to the Conservation of Energy Principle at steady state, $Q_{in} = Q_{out}$, so the equilibrium state can be calculated and the limit of the length liquid nitrogen can flow is as followed:

$$\mathrm{L} = \frac{\mathrm{T_s} - \mathrm{T_{ave}}}{\frac{\ln(\mathrm{D_0}/\mathrm{D_i})}{2\pi \mathrm{k_m}} + \frac{1}{\mathrm{h_c}\pi \mathrm{D_i}} + \frac{1}{\mathrm{h_c}\pi \mathrm{D_o}}} \times \frac{1}{\mathrm{mC_p}(\mathrm{T_{out}} - \mathrm{T_{in}})}$$

## 6.4 Liquid nitrogen cooling in capillary tube

The liquid nitrogen was used to investigate the capillary tube heat transfer. The tube ID of 500 μm and OD of 1000 μm was used in the experiment. Thermocouple was attached to the outer surface of capillary tube at 12.5 cm away from liquid nitrogen source. After the system reached steady state, which was determined on stable temperature reading obtained, the temperature reading on thermocouple was 103 K. That means along with the flowing liquid nitrogen in the tube, the temperature can be sustained from 77 K to 103 K within 125 mm.

Theoretical calculation was also preformed based on the experimental results. Liquid nitrogen inside capillary tube was estimated by average temperature at 90 K ($\mathrm{T_{ave}}$). Air convection on the outer surface of the tube was assumed to be 200 K ($\mathrm{T_m}$). The properties of liquid nitrogen, fused silica and air were taken as shown in Table 6-1, Table 6-3, Table 6-3, respectively. The parameters were combined to obtain the lower and upper limit of final transfer length.

Table 6-1 Properties of liquid nitrogen used in model.

| | Liquid nitrogen[80] | | |
|---|---|---|---|
| Temperature (K) | 77 | 90 | 110 |
| Density (kg/m3) | 807.3 | 745.6 | 621.7 |
| Specific heat (J/kg-K) | $2.051*10^{-6}$ | $2.122*10^{-6}$ | $2.533*10^{-6}$ |
| Viscosity (kg/m-s) | $158*10^{-6}$ | $104*10^{-6}$ | $73*10^{-6}$ |
| Plandtl number | 2.32 | 1.803 | 1.976 |
| Thermal expansion (/K) | 0.00566 | 0.00723 | 0.01394 |
| Thermal conductivity (W/m-K) | 0.1396 | 0.1224 | 0.0936 |

Table 6-2 Properties of fused silica used in model.

| | Fused silica[86] | |
|---|---|---|
| Temperature (K) | 80 | 110 |
| Thermal conductivity (W/m-K) | 0.60 | 0.75 |

Table 6-3 Properties of air used in model.

| | Air[80] | | |
|---|---|---|---|
| Temperature (K) | 150 | 200 | 250 |
| Density (kg/m3) | 2.368 | 1.768 | 1.413 |
| Viscosity (kg/m-s) | $10.28 *10^{-6}$ | $13.29 *10^{-6}$ | $15.99 *10^{-6}$ |
| Plandtl number | 0.756 | 0.739 | 0.722 |
| Thermal expansion (/K) | 0.0067 | 0.0050 | 0.0040 |
| Thermal conductivity (W/m-K) | 0.01374 | 0.01809 | 0.02227 |

In the experiment, the flow rate of liquid nitrogen at steady state is controlled 0.23 m/s via vacuum suction. As shown in Table 6-4, the cooling length of temperature ranging from 77 K to 103 K inside the capillary tube is collected both from experiment and theoretical calculation. Liquid nitrogen cools the fused silica tube below 103 K at a length of 12.5 cm. The upper and lower limits of theoretical calculations are used to compare under different properties. The calculated length ranging from 10.64-13.44 cm exactly contains the actual transfer length of 12.5 cm. Such result confirms the feasibility of the model and is very close to the calculated conditions.

Table 6-4 Comparison of experimental and calculated data.

| | Experiment | | Model | |
|---|---|---|---|---|
| Temperature (K) | 77 | 103 | 77 | 103 |
| Length (cm) | 12.5 | | 10.64-13.44 | |

## 6.5 Expanding the model for liquid nitrogen cooling

In order to expand different flow models for future applications, the temperature change from 77 K to 93 K of liquid nitrogen flows in the laminar (Re<2300) region in the small tube (ID=500 μm, OD=1000 μm) are estimated in Figure 6.4. The mass flow rate increasing from 0 to 80 mg/s in such tube will lead the transfer length of the tube only up to around 0.35 m. In the mean time, the turbulent flow region is also investigated in Figure 6.5. Along with the mass flow rate continuously increasing, the capability of liquid nitrogen transfer far more than laminar region. As we can see, once the mass flow rate can reach 10 m/s based on the velocity axis, the liquid nitrogen achieves a length of around 4.8 m with the same temperature change inside the tube.

The different diameters of the tubes are also investigated based on the model. As shown in Figure 6.6, the different tube sizes (red-ID=0.5 mm, OD=1 mm; blue-ID=1 mm, OD=2 mm; black-ID=2 mm, OD=4 mm) are fully developed. It is obvious that the larger size of the tube, the longer distance will be achieved under the same velocity. When the tube of ID=2 mm, OD=4 mm is used, around 17 m length of liquid nitrogen flow can be obtained at 5 m/s. But it also needs to be aware that the larger size of the tube, the higher mass flow rate will be used.

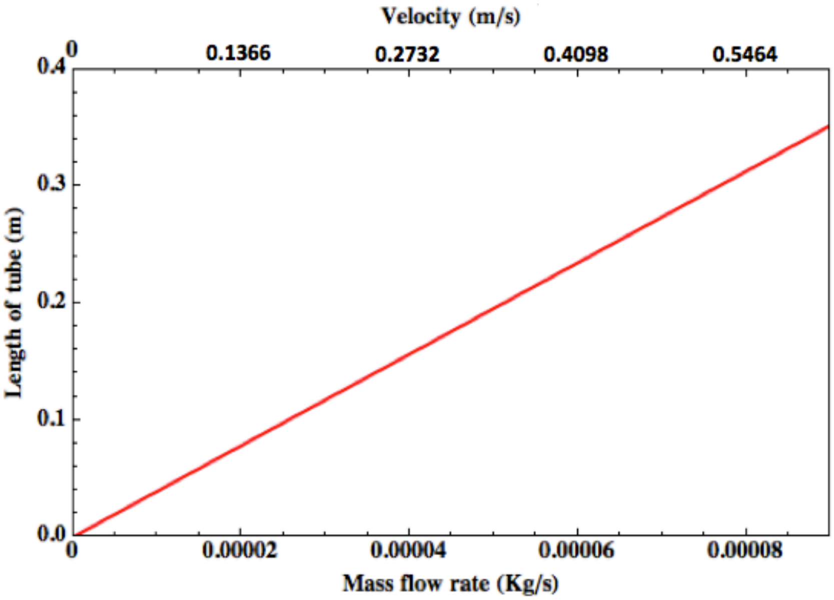

Figure 6.4 Transfer length of LN2 versus mass flow rate in the laminar flow (Re<2300) region: LN2 temperature between 77K to 93 K and tube ID=500 μm, tube OD=1000 μm.

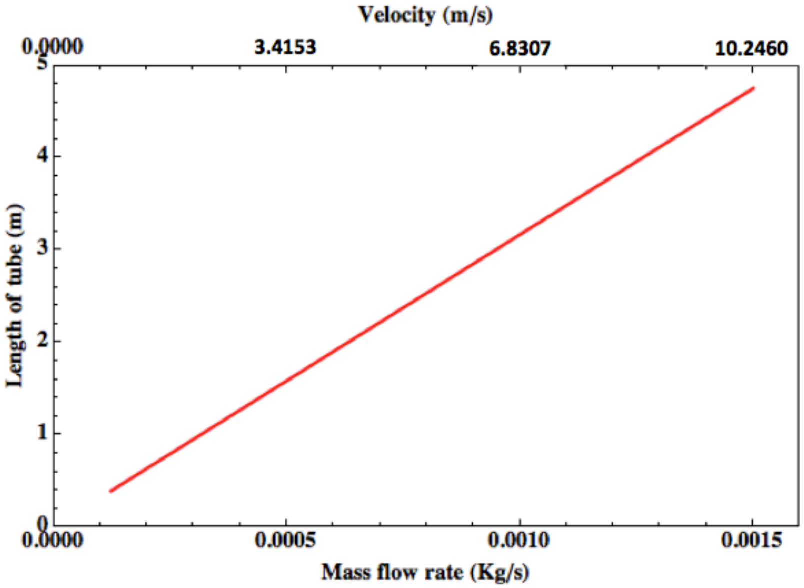

Figure 6.5 Transfer length of LN2 versus mass flow rate in the turbulent flow (Re>3000) region: LN2 temperature between 77K to 93 K and tube ID=500 μm, tube OD=1000 μm.

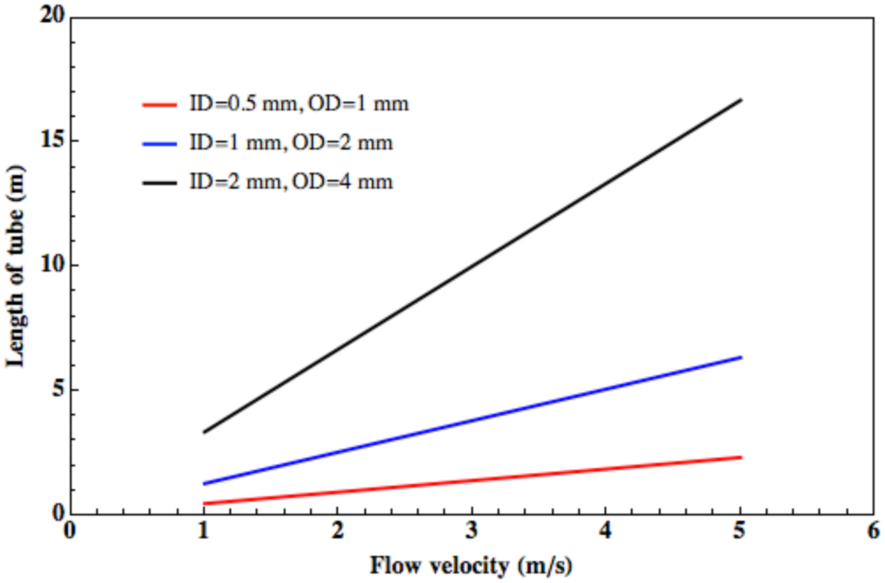

Figure 6.6 Transfer length of LN2 versus flow velocity in the turbulent flow region for different tube diameter:red- ID=0.5 mm, OD=1 mm; blue- ID=1 mm, OD=2 mm; black-ID=2 mm, OD=4 mm. (LN2 temperature between 77K to 93 K)

# 7 Conclusions

In this thesis, Pb and YBCO superconductor core fibers with fused silica cladding have been demonstrated.

The fibers have been fabricated via a melt-draw technique and maintained overall diameters ranging from 200-900 μm and a core diameter of 100-800 μm. A smaller size fiber could also be realized with this technique if required.

Surface morphology analysis confirms that the Pb and YBCO superconductor core fibers possess good circularity and a clean interface between the core and the cladding. Both the Pb and the YBCO core appear dense after the melt-draw process. The melt-draw process avoids contamination during fabrication as shown by the composition analysis.

The YBCO core maintains the appropriate stoichiometric ratio even after the melting process. The elemental mapping detections show that limited cross-diffusion between the Pb core and the fused silica cladding. The YBCO core fiber exhibits some elemental interface effect between the core and the cladding, as well as considerable silicon presents in the core region.

The superconductivity of the Pb core has been verified in liquid helium. YBCO core fiber is also confirmed to be superconductive after heat treatment in $O_2$.

The ordered holey tube structure surrounded the Pb core fiber has exhibited superconductivity with liquid helium cooling through holes.

1-D single-phase steady state model illustrates the heat transfer of liquid nitrogen and considers the natural convection, conduction through the wall and forced convection inside the tube. The results are in reasonable agreement to the experimental results. And the model is also expanded to different conditions.

# 8 Future work

This thesis has proven that it is possible to produce superconductor core fibers with glass cladding via melt-draw process. This may be the first step in the development of truly efficient and cost effective superconducting cables. This technique can be adapted to the other superconductors through proper modification.

The mechanism of how superconductor core and glass cladding interact (only diffusion or reaction) needs further investigation for a comprehensive understanding of mechanism.

The critical current of the superconducting core fiber has not been investigated.

With the help of a draw tower, it may be possible to realize long fiber drawing with better parameter control.

# Reference

1. Fietz, W.H., et al., *Prospects of High Temperature Superconductors for fusion magnets and power applications.* Fusion Engineering and Design, 2013. **88**(6-8): p. 440-445.
2. Alford, N.M., T.W. Button, and J.D. Birchall, *Processing, Properties and Devices in High-Tc Superconductors.* Superconductor Science & Technology, 1990. **3**(1): p. 1-7.
3. Egdell, R.G., W.R. Flavell, and M.S. Golden, *Photoemission-Studies of Oxide Superconductors.* Superconductor Science & Technology, 1990. **3**(1): p. 8-19.
4. Majedi, A.H., *Theoretical Investigations on THz and Optical Superconductive Surface Plasmon Interface.* Ieee Transactions on Applied Superconductivity, 2009. **19**(3): p. 907-910.
5. Stella, F., et al., *Integrating superconductive and optical circuits.* Applied Physics Letters, 2008. **92**(20).
6. Ghamsari, B.G. and A.H. Majedi, *Superconductive, traveling-wave photodetectors: Fundamentals and optical propagation.* Ieee Journal of Quantum Electronics, 2008. **44**(7-8): p. 667-675.
7. Gallop, J.C., *SQUIDS, the Josephson effects and superconducting electronics*. The Adam Hilger series on measurement science and technology. 1991, Bristol, England ; Philadelphia: Adam Hilger. x, 232 p.
8. Dahl, P.F., *Superconductivity : its historical roots and development from mercury to the ceramic oxides*. 1992, New York: American Institute of Physics. xiii, 406 p.
9. Mourachkine, A., *Room-temperature superconductivity*. 2004, Cambridge: Cambridge International Science. 310 p.
10. Cardwell, D.A. and D.S. Ginley, *Handbook of superconducting materials*. 2003, Bristol ; Philadelphia: Institute of Physics Pub.
11. Werfel, F.N., et al., *Superconductor bearings, flywheels and transportation.* Superconductor Science & Technology, 2012. **25**(1).
12. Werfel, F.N., et al., *Recent Up-Scaling in HTS Magnetic Device Technology.* Ieee Transactions on Applied Superconductivity, 2011. **21**(3): p. 1473-1476.
13. Wu, M.K., et al., *Superconductivity at 93-K in a New Mixed-Phase Y-Ba-Cu-O Compound System at Ambient Pressure.* Physical Review Letters, 1987. **58**(9): p. 908-910.
14. Kitazawa, K., *Superconductivity: 100th Anniversary of Its Discovery and Its Future.* Japanese Journal of Applied Physics, 2012. **51**(1).
15. Skakle, J.M.S., *Crystal chemical substitutions and doping of YBa2Cu3Ox and related superconductors.* Materials Science & Engineering R-Reports, 1998. **23**(1): p. 1-40, with permission from Elsevier.
16. Gallagher, P.K., et al., *Oxygen Stoichiometry in Ba2ycu3ox.* Materials Research Bulletin, 1987. **22**(7): p. 995-1006.

17. Jorgensen, J.D., et al., *Structural and Superconducting Properties of Orthorhombic and Tetragonal Yba2cu3o7-X - the Effect of Oxygen Stoichiometry and Ordering on Superconductivity.* Physical Review B, 1987. **36**(10): p. 5731-5734.
18. Cava, R.J., et al., *Structural Anomalies, Oxygen Ordering and Superconductivity in Oxygen Deficient Ba2ycu3ox.* Physica C, 1990. **165**(5-6): p. 419-433.
19. Beyers, R., et al., *Oxygen Ordering, Phase-Separation and the 60-K and 90-K Plateaus in Yba2cu3ox.* Nature, 1989. **340**(6235): p. 619-621.
20. David, W.I.F., et al., *The Structure of the Nonsuperconducting Phase La3ba3cu6o14+X and Its Relation to the High-Tc Superconductor Yba2cu3o7-Delta.* Nature, 1987. **328**(6128): p. 328-329.
21. Cava, R.J., et al., *Oxygen Stoichiometry, Superconductivity and Normal-State Properties of Yba2cu3o7-Delta.* Nature, 1987. **329**(6138): p. 423-425.
22. Namgung, C., J.T.S. Irvine, and A.R. West, *Absence of Critical-Temperature Plateaus in Quenched Samples of Yba2cu3ox.* Physica C, 1990. **168**(3-4): p. 346-350.
23. Maeda, H., et al., *A New High-Tc Oxide Superconductor without a Rare-Earth Element.* Japanese Journal of Applied Physics Part 2-Letters, 1988. **27**(2): p. L209-L210.
24. Kamihara, Y., et al., *Iron-based layered superconductor La[O1-xFx]FeAs (x=0.05-0.12) with T-c=26 K.* Journal of the American Chemical Society, 2008. **130**(11): p. 3296-+.
25. Schilling, A., et al., *Superconductivity above 130-K in the Hg-Ba-Ca-Cu-O System.* Nature, 1993. **363**(6424): p. 56-58.
26. Chu, C.W., et al., *Superconductivity above 150-K in Hgba2ca2cu3o8+Delta at High-Pressures.* Nature, 1993. **365**(6444): p. 323-325.
27. Malozemoff, A.P., et al., *Power applications of high-temperature superconductors: Status and perspectives.* Ieee Transactions on Applied Superconductivity, 2002. **12**(1): p. 778-781.
28. Bray, J.W., *Superconductors in Applications; Some Practical Aspects.* Ieee Transactions on Applied Superconductivity, 2009. **19**(3): p. 2533-2539.
29. Pepe, G.P., et al., *Novel superconducting proximized heterostructures for ultrafast photodetection.* Cryogenics, 2009. **49**(11): p. 660-664.
30. Bednorz, J.G. and K.A. Muller, *Possible High-Tc Superconductivity in the Ba-La-Cu-O System.* Zeitschrift Fur Physik B-Condensed Matter, 1986. **64**(2): p. 189-193.
31. Shi, L., et al., *Study of Photoresponse of High-T-C Y-Ba-Cu-O Superconducting Ultrathin Films Using a Picosecond Laser-Pulse Train.* Applied Physics Letters, 1993. **63**(20): p. 2830-2832.
32. Kwok, H.S., et al., *Nonthermal Optical-Response of Y-Ba-Cu-O Thin-Films.* Applied Physics Letters, 1989. **54**(24): p. 2473-2475.
33. Lindgren, M., et al., *Intrinsic picosecond response times of Y-Ba-Cu-O superconducting photodetectors.* Applied Physics Letters, 1999. **74**(6): p. 853-855.
34. Barone, A.I.f.S.I.W.o.S.P.D. *Superconductive particle detectors : 26-29 October 1987*. Singapore; Teaneck, NJ, USA: World Scientific.

35. Bluzer, N. and M.G. Forrester, *Quantum Detectors in Superconducting Ybco.* Ieee Transactions on Applied Superconductivity, 1995. **5**(2): p. 2583-2586.
36. Bluzer, N. and M.G. Forrester, *Superconducting Quantum Detectors in Ybco.* Journal of Superconductivity, 1994. **7**(2): p. 395-398.
37. Martyniuk, P. and A. Rogalski, *Quantum-dot infrared photodetectors: Status and outlook.* Progress in Quantum Electronics, 2008. **32**(3-4): p. 89-120.
38. Youngdale, E.R., et al., *Auger Lifetime Enhancement in Inas-Ga1-Xinxsb Superlattices.* Applied Physics Letters, 1994. **64**(23): p. 3160-3162.
39. Parker, W.H. and W.D. Williams, *Photoexcitation of Quasiparticles in Nonequilibrium Superconductors.* Physical Review Letters, 1972. **29**(14): p. 924-927.
40. Rothwarf, A. and B.N. Taylor, *Measurement of Recombination Lifetimes in Superconductors.* Physical Review Letters, 1967. **19**(1): p. 27-30.
41. Kinch, M.A., *Fundamental physics of infrared detector materials.* Journal of Electronic Materials, 2000. **29**(6): p. 809-817.
42. Gol'tsman, G.N., et al., *Picosecond superconducting single-photon optical detector.* Applied Physics Letters, 2001. **79**(6): p. 705-707.
43. Robinson, B.S., et al., *781 Mbit/s photon-counting optical communications using a superconducting nanowire detector.* Optics Letters, 2006. **31**(4): p. 444-446.
44. Ghamsari, B.G. and A.H. Majedi, *Rigorous analysis of superconducting multilayer optical waveguides.* Ieee Transactions on Applied Superconductivity, 2007. **17**(2): p. 590-593.
45. Ghamsari, B.G. and A.H. Majedi, *Theory of Superconductive Traveling-Wave Photodetectors.* Ieee Transactions on Applied Superconductivity, 2008. **18**(4): p. 1761-1768.
46. Murata, H., *Handbook of optical fibers and cables*. 2nd ed. Optical engineering. 1996, New York: M. Dekker. xi, 532 p.
47. Senior, J.M., *Optical fiber communications : principles and practice*. 3rd ed. 2008, Harlow: Prentice Hall.
48. Scott, B., et al., *Fabrication of silicon optical fiber.* Optical Engineering, 2009. **48**(10).
49. Scott, B.L., K. Wang, and G. Pickrell, *Fabrication of n-Type Silicon Optical Fibers.* Ieee Photonics Technology Letters, 2009. **21**(24): p. 1798-1800.
50. Scott, B.L. and G.R. Pickrell, *Silicon optical fiber diameter dependent grain size.* Journal of Crystal Growth, 2013. **371**: p. 134-141.
51. Samson, B.N., et al., *Nickel-doped nanocrystalline glass-ceramic fiber.* Optics Letters, 2002. **27**(15): p. 1309-1311.
52. Ballato, J., et al., *Glass-clad single-crystal germanium optical fiber.* Optics Express, 2009. **17**(10): p. 8029-8035.
53. Babu, N.H., et al., *Growth of large sized YBa2Cu3O7 single crystals using the top seeded melt growth process.* Superconductor Science & Technology, 2012. **25**(7).
54. Jin, S., et al., *Fabrication of Dense Ba2ycu3o7-Delta Superconductor Wire by Molten Oxide Processing.* Applied Physics Letters, 1987. **51**(12): p. 943-945.

55. Godeke, A., et al., *State of the art powder-in-tube niobium-tin superconductors.* Cryogenics, 2008. **48**(7-8): p. 308-316.
56. Ma, Y.W., et al., *Development of Powder-in-Tube Processed Iron Pnictide Wires and Tapes.* Ieee Transactions on Applied Superconductivity, 2011. **21**(3): p. 2878-2881.
57. Kumakura, H., et al., *Fabrication and properties of powder-in-tube processed MgB2 tapes and wires.* Journal of Low Temperature Physics, 2003. **131**(5-6): p. 1085-1093.
58. Wong, T. and C.V. Renaud, *Ti and Ta additions to Nb3Sn by the powder in tube process.* Ieee Transactions on Applied Superconductivity, 2001. **11**(1): p. 3584-3587.
59. Renaud, C.V., L.R. Motowidlo, and T. Wong, *Status of powder-in-tube Nb3Sn conductor development at Supercon.* Ieee Transactions on Applied Superconductivity, 2003. **13**(2): p. 3490-3493.
60. Glowacki, B.A., et al., *Superconductivity of powder-in-tube MgB2 wires.* Superconductor Science & Technology, 2001. **14**(4): p. 193-199.
61. Ma, Y.W., et al., *Fabrication and characterization of iron pnictide wires and bulk materials through the powder-in-tube method.* Physica C-Superconductivity and Its Applications, 2009. **469**(9-12): p. 651-656.
62. Mukoyama, S., *Development of YBCO high-Tc superconducting power cables.* Furukawa review, 2009. **35**: p. 1348-1797.
63. Keiser, G., *Optical fiber communications*. 3rd ed. McGraw-Hill series in electrical and computer engineering Communications and signal processing. 2000, Boston, MA: McGraw-Hill. xxi, 602 p.
64. Schultz, P.C., *Fabrication of Optical-Waveguides by the Outside Vapor-Deposition Process.* Proceedings of the Ieee, 1980. **68**(10): p. 1187-1190.
65. Izawa, T. and N. Inagaki, *Materials and Processes for Fiber Preform Fabrication - Vapor-Phase Axial Deposition.* Proceedings of the Ieee, 1980. **68**(10): p. 1184-1187.
66. Nagel, S.R., J.B. Macchesney, and K.L. Walker, *An Overview of the Modified Chemical Vapor-Deposition (Mcvd) Process and Performance.* Ieee Journal of Quantum Electronics, 1982. **18**(4): p. 459-476.
67. Lydtin, H. *Update on fiber manufacture by PCVD*. 1984. Optical Society of America.
68. Lin, Z.C., C.B. Yang, and K.P. Lee, *Theoretical model for the hot-melt-drawn fabrication of optical fibre probes and the analysis of fabrication parameters.* Proceedings of the Institution of Mechanical Engineers Part C-Journal of Mechanical Engineering Science, 2011. **225**(C6): p. 1431-1441.
69. Mawardi, A. and R. Pitchumani, *Optical Fiber Drawing Process Model Using an Analytical Neck-Down Profile.* Ieee Photonics Journal, 2010. **2**(4): p. 620-629.
70. King, F., *Finding the critical temperature of a YBCO superconductor using a voltage probe.* Physics Department, The College of Wooster, 2008: p. 1-4.
71. Ballato, J., et al., *Progress in crystalline semiconductor core optical fibers.* Optical Components and Materials Vii, 2010. **7598**.

72. Ballato, J., et al., *Silicon optical fiber.* Optics Express, 2008. **16**(23): p. 18675-18683.
73. Nicol, J., S. Shapiro, and P.H. Smith, *Direct Measurement of the Superconducting Energy Gap.* Physical Review Letters, 1960. **5**(10): p. 461-464.
74. Garcia-Vazquez, V., et al., *Selected error sources in resistance measurements on superconductors.* Review of Scientific Instruments, 2001. **72**(8): p. 3332-3339.
75. Zhou, L., et al., *The Properties of Ybco Superconductors Prepared by a New Approach - the Powder Melting Process.* Superconductor Science & Technology, 1990. **3**(10): p. 490-492.
76. Gupta, A., et al., *Flux line motion in superconducting (YBa2Cu3O7-d)(1-x)/(SiO2)(x) composite systems in high magnetic fields.* Superconductor Science & Technology, 2007. **20**(10): p. 1084-1091.
77. Atkins, K.R., H. Seki, and E.U. Condon, *Flow of Liquid Helium through Porous Vycor Glass.* Physical Review, 1956. **102**(2): p. 582-583.
78. Mehl, J.B. and W. Zimmermann, Jr., *Flow of Superfluid Helium in a Porous Medium.* Physical Review, 1968. **167**(1): p. 214-229.
79. Eselson, B.N., et al., *Characteristics of the Viscosity of Liquid-Helium Below 1-K.* Jetp Letters, 1980. **31**(1): p. 31-34.
80. Barron, R.F., *Cryogenic heat transfer*. Series in chemical and mechanical engineering. 1999, Philadelphia, PA: Taylor and Francis. xviii, 374 p.
81. Churchill, S.W. and H.H.S. Chu, *Correlating Equations for Laminar and Turbulent Free Convection from a Horizontal Cylinder.* International Journal of Heat and Mass Transfer, 1975. **18**(9): p. 1049-1053.
82. Incropera, F.P. and D.P. DeWitt, *Introduction to heat transfer*. 3rd ed. 1996, New York: Wiley. xxiii, 801 p.
83. Welty, J.R., *Fundamentals of momentum, heat, and mass transfer*. 5th ed. 2008, Danver, MA: Wiley. xiii, 711 p.
84. Incropera, F.P. and D.P. DeWitt, *Fundamentals of heat and mass transfer*. 4th ed. 1996, New York: Wiley. xxiii, 886 p.
85. Gnielinski, V., *New equations for heat and mass transfer in turbulent pipe and channel flow.* Int. Chem. Eng, 1976. **16**(2): p. 359-368.
86. Sviridenko, V.I., et al., *The Thermal-Conductivity of Kv Fused-Silica at 2-300-Degrees-K.* Measurement Techniques Ussr, 1987. **30**(5): p. 454-458.